Supplementary Materials for

Global atmospheric particle formation from CERN CLOUD measurements

Eimear M. Dunne,* Hamish Gordon,*† Andreas Kürten, João Almeida, Jonathan Duplissy, Christina Williamson, Ismael K. Ortega, Kirsty J. Pringle, Alexey Adamov, Urs Baltensperger, Peter Barmet, Francois Benduhn, Federico Bianchi, Martin Breitenlechner, Antony Clarke, Joachim Curtius, Josef Dommen, Neil M. Donahue, Sebastian Ehrhart, Richard C. Flagan, Alessandro Franchin, Roberto Guida, Jani Hakala, Armin Hansel, Martin Heinritzi, Tuija Jokinen, Juha Kangasluoma, Jasper Kirkby, Markku Kulmala, Agnieszka Kupc, Michael J. Lawler, Katrianne Lehtipalo, Vladimir Makhmutov, Graham Mann, Serge Mathot, Joonas Merikanto, Pasi Miettinen, Athanasios Nenes, Antti Onnela, Alexandru Rap, Carly L. S. Reddington, Francesco Riccobono, Nigel A. D. Richards, Matti P. Rissanen, Linda Rondo, Nina Sarnela, Siegfried Schobesberger, Kamalika Sengupta, Mario Simon, Mikko Sipilä, James N. Smith, Yuri Stozhkov, Antonio Tomé, Jasmin Tröstl, Paul E. Wagner, Daniela Wimmer, Paul M. Winkler, Douglas R. Worsnop, Kenneth S. Carslaw†

*These authors contributed equally to this work.
†Corresponding author. Email: hamish.gordon@cern.ch (H.G.); lecksc@ds.leeds.ac.uk (K.S.C.)

This PDF file includes:

Materials and Methods
Figs. S1 to S21
Tables S1 to S7
Caption for Data S1
References

Other Supplementary Material for this manuscript includes the following:
(available at www.sciencemag.org/cgi/content/full/science.aaf2649/DC1)

Data S1

Materials and Methods

1 Overview of CLOUD experiments

The experiments on inorganic nucleation were conducted in 2010, 2011 and 2012 at the CLOUD chamber facility at CERN (Sect. 2 and the Supplementary Material of Ref. (*7*)). In 2010, the binary H_2SO_4-H_2O system was systematically investigated at temperatures between $248\,K$ and $292\,K$ while the ternary H_2SO_4-NH_3-H_2O system was measured at $278\,K$ and $292\,K$ (*7*). The 2011 experiments extended coverage to $208\,K$, with much lower H_2SO_4 (down to $5 \times 10^5\ cm^{-3}$) and NH_3 (below $5\,pptv$) concentrations, to match ambient conditions in the free and upper troposphere. This required much more sensitive instrumentation for the detection of low ammonia levels. Additional data at $278\,K$ were obtained in 2012. The combined results from the three experiments comprise the most complete experimental data of inorganic nucleation so far measured under tropospheric conditions. A more detailed description of the experimental conditions and results can be found in Ref. (*32*).

As well as the organic nucleation rates (*24*), subsets of the inorganic nucleation rates presented in Fig. 1 have been published before. The nucleation rate measurements without added ammonia are presented in Ref. (*31*). In addition, a subset of the data with added ammonia (those data recorded in 2010 at 248 K, 278 K and 293 K) were published in Refs. (*7*) (approximately 20 nucleation rate measurements with added ammonia) and (*23*) (approximately 35 nucleation rate measurements with added ammonia, which mostly overlap with Ref. (*7*)). We add to these data around 100 hitherto unpublished nucleation rate measurements to complete the dataset presented in Fig. 1.

2 CLOUD chamber and instruments

The CLOUD chamber is designed to study in controlled conditions the effect of ionizing radiation and a wide variety of precursor gas concentrations on particle formation, growth and activation to ice or cloud droplets (*7*). It consists of a $3\,m$ diameter electro-polished stainless steel cylinder with a volume of $26.1\,m^3$. Air circulating in the space between the chamber and its thermal insulation controls the internal temperature to a stability of $\pm 0.01\,K$ in the range between 208 and $300\,K$. The temperature can also be raised to $373\,K$ for chamber cleaning by bakeout. More thorough cleaning involves rinsing the chamber walls with ultrapure water and flushing the chamber with air containing high O_3 concentrations. The chamber is filled with N_2 and O_2 from evaporated cryogenic liquids, mixed at a ratio of 79:21, with a pressure of 1.005 atmospheres. Ultra-violet light is used to stimulate photolytic reactions which produce H_2SO_4 in-situ in the presence of O_3, SO_2, O_2 and H_2O. The UV light is fed into the cham-

ber through 250 optical fibres, which avoids perturbing the chamber temperature (*57*). The trace gases SO_2 and (for the ternary runs) NH_3 come from gas cylinders with mixing ratios of $100\,\mathrm{ppmv}$ and 1% respectively, diluted in nitrogen. The flow of the gases into the chamber is precisely regulated by mass flow controllers. Ozone is introduced by illuminating some of the incoming air with UV light ($\lambda < 200\,\mathrm{nm}$) before it reaches the chamber. The absolute humidity is controlled by an air flow through a humidifier, where ultrapure water vapor is added to the flow by means of a Nafion membrane. The humidification system is temperature controlled to $\pm 0.01\,\mathrm{K}$, and the water is purified by re-circulating it through a bank of Millipore Super-Q filters. To suppress contamination of the water through biological activity, it is illuminated by an intense UV light source. The cleanliness of the chamber with regard to nucleation is continually monitored through the use of an Atmospheric Pressure-interface Time Of Flight mass spectrometer (APi-TOF) and a Proton Transfer Reaction Mass Spectrometer (PTR-MS). Two fans, one installed at the bottom of the chamber and another at the top, continuously mix the contents of the chamber by operating in a counter-flow mode (*58*). The mixing fans are driven by magnetically coupled motors installed outside the chamber.

3 Ion production and control

To replicate the galactic cosmic-ray (GCR) intensity from ground level to the stratosphere, the chamber can be exposed to a $3.5\,\mathrm{GeV/c}$ secondary π^+ beam from the CERN Proton Synchrotron. The beam is defocused to cover a cross-section of the chamber with area about $1.5 \times 1.5\,\mathrm{m}^2$, leading to an ion pair production rate between approximately 3 and $110\,\mathrm{cm}^{-3}\mathrm{s}^{-1}$. Natural GCRs lead to an ion pair production rate of $1.5-3\,\mathrm{cm}^{-3}\mathrm{s}^{-1}$ (depending on temperature) when the beam is off. The intensity and angular distribution of the GCRs are measured next to the chamber using an ionization-counter array, while the beam profile is monitored by a plastic scintillator hodoscope close to the chamber and a separate pair of scintillation detectors in front of the beam aperture. Neutral (ion-free) conditions are achieved by applying an electric field of up to $20\,\mathrm{kV/m}$ between two electrodes positioned near the top and bottom of the chamber. This sweeps all small ions from the chamber within about $1\,\mathrm{s}$. This configuration allows us to measure nucleation rate under three ionization conditions: pion beam (J_π), galactic cosmic rays alone (J_{gcr}), and neutral (J_n) (*7*).

4 Measurement sequence

To measure a nucleation rate, the chamber is cleaned of any existing aerosol and the gas concentrations, temperature and relative humidity needed for the experiment are established. If

required, the electric field or pion beam are switched on to remove or produce extra ions respectively. Ultraviolet light is then permitted to enter the chamber to generate sulfuric acid. Once sufficient H_2SO_4 is present, nucleation starts. After reaching stable conditions with the clearing field present, the neutral nucleation rate is measured. The electric field is then switched off and the nucleation rates measured with the same gas concentrations under GCR or pion beam conditions. Finally the run is ended by closing the UV shutter and clearing aerosol from the chamber in preparation for the next experiment. The procedure usually takes around six hours for a single run under fixed gas conditions.

5   Sulfuric acid concentrations

For data recorded in 2010 and 2011, the sulfuric acid concentration was measured with a quadrupole Chemical Ionization Mass Spectrometer (CIMS, e.g. Ref. (*59*)) in 2010 and 2011. The instrument is calibrated in the laboratory as described in Ref. (*60*) and compared to measurements with a chemical ionization time of flight mass spectrometer (CI-APi-TOF, (*61*)) in 2012. The monomer concentration determined by the CIMS is equal to (*62*)

$$[H_2SO_4] = \frac{C}{L} \ln \left(1 + \frac{CR_{97}}{CR_{62}} \right)$$

where CR_{62} is the count rate for the primary nitrate ion, which has mass/charge ratio 62, CR_{97} is the count rate of the HSO_4^- ion, L, around 0.3, is the fraction of sulfuric acid that passes through the sampling line without interacting with the walls, and C is derived from the calibration and is $1 \times 10^{10}\,\mathrm{cm}^{-3}$ (*60*).

As a cross check, the total sulfuric acid concentration was also calculated from the ozone, SO_2 and water concentrations using literature reaction rates (*63*) with a free parameter for the photolysis rate. The photolysis rate is almost independent of temperature and therefore the low-temperature sulfuric acid concentrations are determined by calibrating this mechanism with the measured concentrations at high temperatures. This indirect method accounts for all sulfuric acid clusters as well as monomers but is likely to be less precise. The difference between modeled and measured concentrations is found to be within $-33\%/+50\%$ in 77% of 254 nucleation runs studied. This range is therefore considered to be an estimate of the uncertainty on the sulfuric acid concentrations for the inorganic nucleation measurements. The uncertainty is slightly larger than that in the monomer concentration in Ref. (*62*) as the number of experimental campaigns used in this study is greater.

6 Ammonia mixing ratios

In 2010, ammonia concentrations were measured with a long-path absorption photometer (LOPAP) at 278 K and 292 K . This instrument has a lower detection limit of $\sim 35\,\mathrm{pptv}$ (*64*). The 2010 experiments therefore focused on higher NH_3 concentrations up to $1400\,\mathrm{pptv}$. During 2011 and 2012, much lower NH_3 concentrations were necessary and a more sensitive ion chromatograph (IC) was used, which could measure NH_3 down to mixing ratios of around $1\,\mathrm{pptv}$ (*65*). Both measurement techniques rely on dissolving gas phase NH_3 in liquid water and can only be applied at temperatures above $0\,^{\circ}\mathrm{C}$. Since most runs in 2011 were conducted below $0\,^{\circ}\mathrm{C}$, a relationship was derived between the flow of NH_3 going into the chamber through the mass flow controllers and the NH_3 mixing ratio measured by the IC. The measurements were carried out at $278\,\mathrm{K}$ during a dedicated calibration period at the end of the 2011 campaign (*32*). A further measurement of $[NH_3]$ was obtained from the PTR-MS, but instrumental problems during 2011 meant that it did not contribute a complete time series. However, for a certain period it did yield reliable measurements at $223\,\mathrm{K}$ while NH_3 was being added to the chamber. The PTR-MS measurements at $223\,\mathrm{K}$ agree with the NH_3 concentrations derived from the mass flow controller (MFC) settings that are calibrated against the IC measurements above $273\,\mathrm{K}$. This validates the derivation of NH_3 concentrations from the MFC settings over a wide temperature range, within the following experimental uncertainty. At high NH_3 mixing ratios (above approximately $5\,\mathrm{pptv}$ at the lowest temperatures and around $100\,\mathrm{pptv}$ at the highest temperatures), the uncertainty on the mixing ratio is very small, estimated as $\pm 20\%$. However, at low NH_3 mixing ratios, the uncertainty is larger due to the contribution of NH_3 background contamination. At $278\,\mathrm{K}$, the background mixing ratio during 2011 was measured as $2\,\mathrm{pptv}$ with $-50\%/+100\%$ uncertainty. For the lower temperatures, there is no direct background measurement. However, using the measurement at $278\,\mathrm{K}$, background NH_3 can be estimated at other temperatures on the assumption it originates from desorption from surfaces. This yields background estimates of $2.5 \times 10^5\,\mathrm{cm}^{-3}$ or $0.012\,\mathrm{pptv}$ at $208\,\mathrm{K}$, with a factor 10 uncertainty, and $1.0 \times 10^7\,\mathrm{cm}^{-3}$ or $0.4\,\mathrm{pptv}$ at $248\,\mathrm{K}$. The details of the method for deriving the calibration curve and the background NH_3 mixing ratios are described in a separate paper (*32*). In general, the uncertainty in the mixing ratio of NH_3 is around $\pm 20\%$ at $100\,\mathrm{pptv}$ and above, $-50\%/+100\%$ for ratios of $1 - 10\,\mathrm{pptv}$, and up to a factor of 10 at lower values, with a temperature dependence as described earlier. The parameterization of nucleation rates is insensitive to NH_3 mixing ratios below $0.1\,\mathrm{pptv}$ since inorganic nucleation becomes pure binary at these values.

To investigate pure binary nucleation and ternary nucleation with ammonia, the 2011 campaign was divided into two periods. In the first period no NH_3 was intentionally introduced into the chamber, while during the second period NH_3 was added to the chamber through a mass flow control system.

The molecular composition of the charged nucleating clusters was measured with an APi-TOF during each experimental run. This allowed unambiguous verification of the amount of ammonia or organic species in, or their absence from, the charged nucleating clusters (*34, 35*). The APi-TOF spectra show that for ternary NH_3-nucleation, when the molar concentration ratio $[NH_3]/[H_2SO_4]$ is greater than 1, ammonia is found in almost all negatively charged clusters that contain four or more sulfur atoms ($HSO_4^-.(H_2SO_4)_n(NH_3)_m$, $n \geq 3$, $m \geq 1$). However, when $[NH_3]/[H_2SO_4]$ is below 0.1, the clusters containing no NH_3 dominate the mass spectrum and NH_3 is almost entirely absent – see Fig. S1 (*34, 66*). Positively charged clusters are only seen at high $[NH_3]/[H_2SO_4]$ (*34*) and grow more slowly than negative clusters (*66*). They are assumed not to contribute significantly to ion-induced nucleation rates, so the ion-related parameterizations described in Sect. 8 consider only the negative ion concentration. The mass spectra were used in 2011 to indicate the influence of ternary compounds on nucleation for the experiments where no ammonia was added (*7*). For almost all experiments that were intended to be binary, no contamination was identified. For the development of the parameterization of nucleation rates, the background NH_3 concentration appropriate for the measured temperature was assumed.

During the second half of the 2011 experimental campaign, measurements at different temperatures were performed and the ammonia concentration was varied at each temperature. After nucleation measurements in which NH_3 was added to the chamber, sufficient time was allowed for the NH_3 to decay away before restarting measurements without NH_3. During the transition periods to new temperatures and measurements without NH_3, the lines supplying ammonia to the chamber were continuously flushed with ammonia to keep the pipes conditioned, but the flow was vented through a valve just before the inlet into the chamber so that no NH_3 reached the chamber. Measurements were performed to indicate that the influence of contaminant ammonia from previous experiments is negligible by comparing the nucleation rates with the pure binary situation before any NH_3 was added to the chamber.

7 Nucleation and growth rate evaluation

Nucleation rates J are reported at a mobility diameter of $1.7\,nm$, in accordance with previously published results from the CLOUD experiment (*7, 24*). Strictly, this is the formation rate of particles at $1.7\,nm$, rather than the nucleation rate, since this diameter does not necessarily correspond to the critical cluster size at all temperatures and precursor concentrations. Classical binary nucleation theory shows that the critical cluster is smaller at low temperatures and that nucleation can even become barrierless (*31*). Experimentally, it would be more straightforward to determine the formation rate at a larger particle diameter, for example $3\,nm$. However, the survival probability between $1.7\,nm$ and $3\,nm$ in the CLOUD chamber is low, often below 10%,

while it is higher in the cold free troposphere since the condensation sink there is lower than the CLOUD wall loss rate. Therefore the formation rate at $1.7\,\mathrm{nm}$ in CLOUD will be a closer representation of particle formation at the corresponding size in the free troposphere than that at $3\,\mathrm{nm}$.

The nucleation rates reported here have been evaluated from a TSI 3776 condensation particle counter (CPC) with a cut-off diameter of $3.2\,\mathrm{nm}$, then corrected back to $1.7\,\mathrm{nm}$. Additional CPCs (two particle size magnifiers (PSMs) and two diethylene glycol CPCs) which have cut-off diameters between 1.2 and $2.0\,\mathrm{nm}$ were also used to cross-check the result obtained from the TSI 3776 CPC. Since the detection efficiencies are not a step function at the cut-off size, particles with diameters below this size are also detected to some extent by all of these counters. For some experimental conditions, particles below the critical size in the counters with the smallest cut-offs may be detected, leading to an over-estimation of the nucleation rate. In most cases, however, the nucleation rates derived from these sub-$2\,\mathrm{nm}$ counters are consistent with the value of $J_{1.7}$ derived from the TSI 3776 CPC. For measurements at low temperatures ($208\,\mathrm{K}$ or $223\,\mathrm{K}$ in the chamber), the counters were housed in thermally insulated boxes which were cooled to $243\,\mathrm{K}$. Since the instruments are warmer than the chamber, it is likely that some small particles will evaporate and will therefore not be counted. It is not possible to fully quantify the losses involved, but a first attempt to characterize the effects of temperature on the counters is described in Ref. (*67*).

The formation rates are obtained from dN_{CPC}/dt where N_{CPC} is the concentration measured in the CPC. Before calculating $J_{1.7}$, the measured concentrations are corrected in a two-step process (*68*): first the concentrations are corrected by integrating the loss of particles above the detection threshold of $3.2\,\mathrm{nm}$ due to dilution, wall loss and coagulation; second, the same loss processes that have occurred during the growth of particles from $1.7\,\mathrm{nm}$ to $3.2\,\mathrm{nm}$ are accounted for. The second correction requires knowledge of the particle growth rate (GR). This is experimentally determined from the different rise times at which CPCs with different cut-off diameters start detecting newly formed particles. The instruments used to evaluate GRs were the two PSMs, the di-ethylene glycol CPCs, a scanning mobility particle sizer (nano-SMPS) and a neutral air ion spectrometer (NAIS). The nano-SMPS measures particles in a size range from approximately 5 to $100\,\mathrm{nm}$, and the NAIS measures ions in the range $0.8 - 42\,\mathrm{nm}$ and total particle populations in the range $2.5 - 42\,\mathrm{nm}$ (*69*). Since GR measurements were not always available for the same time intervals as those used for the nucleation rate calculations, a parameterization was derived which allowed us to calculate the growth rate for each experimental run (*32*). The particle size spectra measured with the nano-SMPS allows particle losses due to the coagulation sink to be determined, although these are usually small compared to losses to the chamber walls. When correcting for losses between 1.7 and $3.2\,\mathrm{nm}$, some simplifying assumptions were made which enable formation rates to be determined consistently in diffi-

7

cult cases, for example where the nucleation rate is low or when the nucleation processes are at steady state for only a short time. The main simplification is to approximate the change in formation rate from 3 to $1.7 \, \text{nm}$ as a linear function of growth and loss rates. The accuracy of this approximation is determined by calculating as many nucleation rates as possible according to the prescription of Ref. (*70*), which requires a longer period of nucleation at steady state than the approximate method. The rates calculated with the two techniques are compared in Fig. S2. Most of the data that are grouped below the 1:1 line in the figure were taken in 2011, where there is an uncertainty on the wall loss rate since the flows in the chamber were changed following the introduction of a hood around the fans after these experiments. The systematic uncertainty associated with the procedure is found to be a factor of 2.5 overall. This uncertainty usually dominates the uncertainty on each nucleation rate data point shown in Fig. S2, which is determined by combining the uncertainties associated with the growth rates, particle counts, and loss rates, and therefore the factor 2.5 is used in subsequent analysis (Sect. 19). However, the uncertainty in the nucleation rate measurement is less significant overall than uncertainties in the sulfuric acid and ammonia concentrations.

8 Nucleation rate parameterization

In the global aerosol model, the overall nucleation rate is given by the sum of the following individual processes:

$$J_{b,n} = k_{b,n}(T)[\text{H}_2\text{SO}_4]^{p_{b,n}}$$
$$J_{t,n} = k_{t,n}(T)f_n\left([\text{NH}_3], [\text{H}_2\text{SO}_4]\right)$$
$$J_{b,i} = k_{b,i}(T)n_-[\text{H}_2\text{SO}_4]^{p_{b,i}}$$
$$J_{t,i} = k_{t,i}(T)n_-f_i\left([\text{NH}_3], [\text{H}_2\text{SO}_4]\right)$$
$$J_{org} = k_{t,org}[\text{BioOxOrg}][\text{H}_2\text{SO}_4]^2$$

where $J_{b,n}$ is the binary neutral rate, $J_{b,i}$ is the binary ion-induced rate, $J_{t,n}$ is the ternary neutral rate, $J_{t,i}$ is the ternary ion-induced rate, J_{org} is the ternary organic rate, n_- is the steady state concentration of small negative ions, and $[\text{H}_2\text{SO}_4]$, $[\text{BioOxOrg}]$ and $[\text{NH}_3]$ are gas concentrations (cm^{-3}). BioOxOrg and the characteristics of the organic nucleation are described later in this Section. The ternary organic rate can be further split into neutral and ion-induced components, but with a larger uncertainty than in the inorganic case as we have fewer measurements. The dataset of inorganic nucleation rate measurements was fitted to the first four of these equations, while the organic nucleation rate was determined according to the final equation, in accordance with Ref. (*24*). Uncertainties in the parameterization are discussed in subsequent sections, particularly Sect. 19.

In the inorganic parameterization, the 20 free parameters contained within the first four of

the equations above (described in more detail later in this Section) are fitted using the min-pack.lm interface to the Levenberg-Marquardt algorithm (*71*) in R. Alternative fit methods (Nelder-Mead, conjugate-gradient and quasi-Newton) were also tried, together with a strategy of running all methods in a loop. The optimisation is designed to find the best value of the R^2 coefficient.

Since an *ab initio* fit of 20 free parameters is not feasible, the fit of the free parameters begins with binary neutral nucleation only. Assuming for now that the runs without added ammonia are pure binary, the four free parameters (three temperature coefficients and one power of the sulphuric acid concentration) are fitted. Next, the ternary neutral data are added (two powers, three temperature coeffcients and the a_n parameter described below). The data are fitted first with the binary parameters fixed, then with them floating, which allows the binary parameters to re-adjust for a nonzero contribution from ternary nucleation in the runs without added ammonia. Binary ion-induced nucleation is then added, followed by ternary ion-induced nucleation. All the ion-induced nucleation parameters are then refitted, followed by a final step in which all parameters are allowed to vary together. The final fit was re-run many thousands of times with large perturbations to the starting fit parameters to check that the optimizations had reached a global minimum. The R^2 value is 0.90 and the residuals of the nucleation rates with respect to the parameterization are shown in Fig. S3. The values of the fit parameters, which are explained in more detail below, are given in Table S1.

To account for the temperature dependence of the inorganic J, the rate coefficients $k(T)$ are empirical, and have the form

$$\ln k_{(x,y)} = u_{(x,y)} - \exp\left(v_{(x,y)}\left(\frac{T}{1000} - w_{(x,y)}\right)\right),$$

where $u_{(x,y)}$, $v_{(x,y)}$, and $w_{(x,y)}$ are fitted coefficients. The subscript x refers to binary or ternary nucleation ($J_{b/t,y}$) and y to neutral or ion-induced components ($J_{x,n/i}$). The strong temperature dependence found in the data is in good qualitative agreement with quantum chemistry calculations (*23, 72*). The double exponential form with its three free parameters per coefficient is complex, but leads to the best overall R^2 value, of 0.9. Single exponential functions of the form

$$\ln k_{(x,y)} = u_{(x,y)} - v_{(x,y)}\left(\frac{T}{1000}\right)$$

were also tried but led a poorer overall agreement with the data, $R^2 = 0.83$. Since this optimisation contains four fewer free parameters, the poorer agreement with the data does not necessarily mean the fit is worse. We therefore consider the variation between this fit result and the baseline fit to be a useful measure of uncertainty in the parameterization, particularly in the temperature dependence. Therefore the fit parameters are given in Table S2. The parameters other than u, v and w can be directly compared to the baseline fit parameters; the dependence

9

of the nucleation rates on vapor concentrations is reduced slightly (but not substantially) when this temperature parameterization is used. The results of running the global simulation with this second parameterization are described in Sect. 19.

At high ammonia concentrations, the inorganic ternary nucleation rate was found to depend approximately linearly on $[NH_3]$. However, at very low concentrations a small addition of ammonia caused a much sharper increase of nucleation rate with ammonia concentration, as the clusters changed from pure binary to ammonia ternary. This indicates a dependence of the nucleation rate on ammonia that is initially steep but then flattens at higher concentrations, with the transition region depending on $[NH_3]/[H_2SO_4]$ (see Fig. 5 in Ref. (*34*)). Cluster models (*73*) and mass spectrometry measurements from CLOUD (*34*) suggest that ammonia readily evaporates from the smallest charged clusters, with a strong dependence on the number of H_2SO_4 molecules in the cluster and temperature. From Fig. S1, with approximately $2\,ppt$ of NH_3 and a typical H_2SO_4 concentration of 4×10^8, ion-induced nucleation is clearly mostly binary. We assume that neutral nucleation is binary when ion-induced nucleation is observed to be binary under the same conditions. Qualitatively, this is expected since neutral sulfuric acid dimers or trimers are relatively unstable. Therefore, at low concentrations of ammonia, ternary neutral nucleation is likely to be inhibited because new sulfuric acid clusters will often evaporate before an ammonia molecule arrives to stabilize them. The uncertainty associated with this assumption is studied in Sect. 19 by refitting the parameterization with binary neutral nucleation constrained to be zero (which gives an R^2 value of 0.88). It is also expected that, at a given ammonia concentration, the ternary nucleation pathways will eventually saturate with respect to sulfuric acid. To capture these three aspects of the behaviour of the ternary nucleation pathways, the function $f([NH_3], [H_2SO_4])$ is used:

$$f_y([NH_3], [H_2SO_4]) = \frac{[NH_3][H_2SO_4]^{p_{t,y}}}{a_y + \frac{[H_2SO_4]^{p_{t,y}}}{[NH_3]^{p_{A,y}}}}$$

where y is n for the ternary neutral pathway and i for the ternary ion-induced pathway. The behaviour of this formula depends on the denominator. When

$$a_y << \frac{[H_2SO_4]^{p_{t,y}}}{[NH_3]^{p_{A,y}}}$$

then

$$f_y([NH_3], [H_2SO_4]) \sim [NH_3]^{1+p_{A,y}}.$$

Thus, when sulfuric acid is in excess, nucleation will be mostly binary and the ternary contribution is limited only by the ammonia concentration. On the other hand, when

10

$$a_y >> \frac{[\text{H}_2\text{SO}_4]^{p_{t,y}}}{[\text{NH}_3]^{p_{A,y}}}$$

then

$$f_y([\text{NH}_3], [\text{H}_2\text{SO}_4]) \sim \frac{[\text{NH}_3][\text{H}_2\text{SO}_4]^{p_{t,y}}}{a_y}.$$

Therefore, when ammonia is in excess, the nucleation rate depends only weakly (linearly) on its concentration and has a much stronger dependence (approximately cubic) on sulfuric acid. For ternary neutral nucleation with high but atmospherically relevant sulphuric acid concentrations of around $10^7\,\text{cm}^{-3}$, this condition is met whenever ammonia concentrations are above around $1\,\text{ppt}$ due to the high value of $p_{A,n}$, while for ternary ion-induced nucleation $p_{A,i}$ is comparable to $p_{t,i}$ so its value is more dependent on the sulphuric acid concentration. Since this functional form would in principle allow nucleation rates to increase beyond the kinetic limit set by sulfuric acid collisions at very high ammonia concentrations, any J rates in the aerosol model that reach the kinetic limit in Ref. (*70*) are set equal to that limit. This constraint is rarely reached so has no significant effect. Fig. S4 shows how the function works in practise. Since the uncertainty in our measured $[\text{NH}_3]$ depends on its value (the relative uncertainty is larger at low concentrations, see Sect. 6) we re-fit the parameterization in scenarios of overestimated and underestimated chamber ammonia. The optimization leads to $R^2 = 0.89$ in the low-ammonia case and $R^2 = 0.88$ in the high-ammonia case. The results of rerunning the global model in these scenarios are given in Sect. 19.

Figure S5 shows the parameterized nucleation rates as a function of ammonia and sulfuric acid at five important temperatures (208, 223, 248, 273, and 292 K), together with measured nucleation rates. Atmospheric concentrations of ammonia and sulfuric acid derived from the global model (Sect. 12) are indicated in this figure as greyscale density distributions. Fig. S5 shows that the experimental data points were recorded under conditions close to those most important in the atmosphere, to minimize the need for extrapolation using the parameterization. At higher temperatures this becomes more challenging for inorganic nucleation because the minimum nucleation rate that can be measured reliably in CLOUD is around $10^{-3}\,\text{cm}^{-3}\text{s}^{-1}$. However, such low nucleation rates do not produce significant numbers of particles in the model at high temperatures due to high coagulation sinks at the low altitudes that correspond to these temperatures, hence the lack of nucleation predicted in the tropical marine boundary layer (Fig. S11 in Sect. 12).

The nucleation rates are compared to predictions of the ACDC model in Ref. (*32*). The decrease in the ternary inorganic nucleation at low ammonia concentration is steeper than the model predicts, but the overall characteristic is qualitatively similar. Moreover, close agreement

11

is not expected since the ACDC model has a large uncertainty and the fit presented here is not well constrained at low ammonia concentrations, as discussed in Sect. 19.

The negative small ion concentration, n_- was calculated from the steady state solution to the equation

$$\frac{dn_-}{dt} = q - \alpha(T)n_-^2 - Xn_-,$$

where q is the ionization rate, α is the recombination coefficient, and X is the loss rate of ions due to scavenging and to ion-induced nucleation itself.

The ionization rate is calculated from the intensity of the beam as measured by the scintillation counters (Sect. 3) and from the GCR ion pair production rate of $1.8\,\mathrm{cm^{-3}s^{-1}}$ at 298 K. The ionization rate is adjusted to account for the air density variation with temperature. The recombination coefficient of Brasseur and Chatel (74) was found to give the best representation of separate CLOUD experimental measurements in Ref. (33). It takes the form

$$\alpha = (6 \times 10^{-8})\sqrt{(300/T)} + (6 \times 10^{-26})\,[M_{\mathrm{air}}]\left(\frac{300}{T}\right)^4 \tag{1}$$

where $[M_{\mathrm{air}}]$ is the concentration of air molecules in $\mathrm{cm^{-3}}$. The linear ion loss rate is given by

$$X = \frac{1}{\tau_i} + \frac{J_{b,i} + J_{t,i}}{n_-},$$

where τ_i is the ion lifetime in the chamber without nucleation, assumed to correspond to the lifetime with respect to the chamber walls of sulfuric acid, equal to $480\,\mathrm{s}$. It is assumed that only negative ions participate in nucleation (see Sect. 6). The steady state concentration of small ions is therefore

$$n_- = \frac{\sqrt{(X^2 + 4\alpha q)} - X}{2\alpha}.$$

When losses due to pre-existing aerosol, the chamber walls, and ion-induced nucleation are negligible, $X \to 0$ and $n_- \to \sqrt{(q/\alpha)}$. When losses due to recombination are small compared to linear loss processes, as is the case when nucleation rates are high, n_- can be approximated by q/X. The total ion-induced nucleation rate saturates at the ionization rate, since the number of particles nucleating on ions in steady state cannot exceed the ion production rate. The formulation constrains the ion-induced nucleation rates to satisfy $J_{b,i} + J_{t,i} \leq q$.

The organic nucleation rate is determined as in Ref. (24). The experiments at CLOUD were performed using pinanediol (PD) as a precursor. The concentration of the nucleating oxidation products of PD is inferred from the reaction rates of pinanediol with hydroxyl radicals. The BioOxOrg referred to in Ref. (24) is the first-generation oxidation product of pinanediol with

hydroxyl radicals. In the global model, BioOxOrg is assumed to be equivalent to the oxidation products of alpha-pinene that participate in nucleation, as described in the Supplementary Information of Ref. (*24*). The temperature dependence of the organic nucleation rate is not known from CLOUD experiments, but an upper bound on the strength of the dependence is estimated from quantum chemical calculations, described in Sect. 10 below.

The ion-induced fraction of organic nucleation was measured in Ref. (*24*) at 278 K to be approximately 50% for most nucleation rates below the ion production rate limit. With beam, the ion pair production rate increases by approximately a factor 30, and the ion concentration by a factor of approximately five due to the square root dependence described earlier. This factor of five can be seen in the inorganic parameterization in Fig. 2. For GCR conditions, ternary inorganic nucleation at 278 K and low nucleation rates, below the saturation at the ion production rate, is at least 80% ion-induced. The enhancement of the organic nucleation rate is much weaker (*24*). The representation of organic ion-induced nucleation in the global aerosol model is described in Sect. 15.

9   Humidity dependence of nucleation rates

Nucleation rates are expected to show a significant dependence on relative humidity (RH) (*75*) and this appears to be borne out by observations (*46*). The limited number of CLOUD nucleation measurements did not allow the RH dependence of nucleation to be fully integrated into our parameterization as a fifth dimension, although it can be parameterized on a more ad-hoc basis (see below). Most experiments were performed at an RH of 38%. The dependence of the inorganic nucleation rates on RH was measured at 208, 223 and 298 K. Fig. S6A shows the humidity dependence of the nucleation rate at 223 and 208 K, and Fig. S6B that at 298 K.

In our model, the inorganic system is assumed to be saturated with respect to RH above values of 10%. For the purposes of our inorganic nucleation parameterization, we therefore assume that no nucleation occurs below 10% RH, and nucleation is otherwise independent of humidity. As a sensitivity study, we included a temperature-dependent factor that models the RH dependence of the inorganic nucleation rate with a polynomial function. The empirical function we used is $K_{RH} = 1 + c_1(RH - 0.38) + c_2(RH - 0.38)^3(T - 208)^2$ for constant c_1 and c_2, with the constraint that K_{RH} is set to zero if it is less than zero. Here RH is expressed as a fraction. The parameters of this function $c_1 = 1.5 \pm 1.3$ and $c_2 = 0.045 \pm 0.003$ were determined by fitting the ratio of the parameterized and measured nucleation rates (similar to the strategy employed to plot Fig. S6) as a two-dimensional function of temperature and relative humidity. Since we do not consider any biases that may be introduced by fitting the ratio of measured and parameterized rates rather than the nucleation rates themselves, this parameterization is not included in our main results. A 0.7% change in the concentration of $70\,\mathrm{nm}$ diameter particles

at cloud-base level is found when this function is applied to the binary nucleation rate with the ternary rates unchanged.

The RH dependence of the organic nucleation rates was not investigated in Ref. (*24*) and is not accounted for in the model by default. Including the dependence on RH for ternary nucleation (organic and inorganic), we obtain an increase in 3 nm particle concentrations at cloud level of 34.0% averaged globally. This leads to an 6.0% increase in CCN. This is relatively homogeneously distributed across the globe (Fig. S7). The change of 34% is on the same scale as the seasonal differences between modelled and observed particle concentrations when averaged over surface sites (Sect. 18). Well above the clouds, the increase is much lower: while the water concentration is substantially less at these high altitudes, the relative humidity does not change substantially. Thus at an altitude of around $6.7 \, \mathrm{km}$, the change in the concentration of $3 \, \mathrm{nm}$ particles is only 14%, and the average change for the whole troposphere is also 14%. The effects on CCN are smaller than those on the number of ultrafine particles, as expected and shown in Fig. S8. Unfortunately, consideration of the influence of sub-grid meteorology which could also affect nucleation (*44, 46*) is also not practical in the present study.

10 Quantum chemistry simulations

Since experimental measurements are lacking, the temperature dependence of ternary organic nucleation was estimated with model studies based on quantum chemical calculations of cluster binding energies. The organic proxy compound 3-methyl-1,2,3-butane-tricarboxylic acid (MBTCA) was chosen because it is one of the few well known compounds formed in oxidation of volatile organic compounds that have a high O:C ratio. In addition, there are formation free energies already available from previous works (Supplementary Materials of Ref. (*24*)) for MBTCA-sulfuric acid clusters. The reported formation Gibbs free energies are calculated at $278 \, \mathrm{K}$. To study the temperature dependence of the MBTCA-sulfuric acid nucleation rates, the vibrational frequencies calculated using the method proposed in Ref. (*72*) were used to re-calculate the thermodynamic contributions at different temperatures. As in Ref. (*24*), water molecules were not included in the calculations.

These formation Gibbs free energies were used in the Atmospheric Cluster Dynamics Code model (ACDC), described in detail in Ref. (*76*), to derive the nucleation rate of MBTCA-sulfuric acid system at different temperatures. The ACDC model has been used successfully to interpret different experimental observations (*23, 77*).

To simulate steady-state conditions, the monomer concentrations and the total concentration of acid are fixed and the simulation is run until concentrations and formation rates no longer change with time. In this study the concentration of MBTCA is kept constant at $1 \, \mathrm{pptv}$ while that of sulfuric acid is varied between 10^5 and $10^8 \, \mathrm{cm}^{-3}$. The available quantum chemistry data

is limited to neutral clusters containing two sulfuric acid and two MBTCA molecules. Therefore only neutral nucleation is simulated and it is assumed that any cluster with two sulfuric acid and two MBTCA molecules (2,2) is representative of a nucleated cluster. The critical steps in nucleation are considered likely to be these first steps, but this approximation nevertheless introduces a large uncertainty. The calculated temperature dependence of the nucleation for different sulfuric acid concentrations is represented in Fig. S9. The effect of this temperature dependence on the modeled particle concentrations is discussed in Sect. 20.

As stated in the main text, this estimation is likely to lead to a stronger temperature dependence than the reality because the isomerization reactions that create organic molecules with sufficiently low volatility to participate in nucleation are slower at low temperature (*36*). Therefore the oxidation level will decrease, because, instead of isomerization, organic peroxy radicals will react with other peroxy radicals to create stable, less oxidized species. Therefore we also perform simulations with a plausible weaker temperature dependence, which lies between the extrema of zero temperature dependence and this strong dependence:

$$J'_{org} = J_{org} \exp(-(T - 278)/10) \tag{2}$$

The results are also given in Sect. 20.

11   Global aerosol model

We used the GLOMAP aerosol microphysics model (*4, 13, 78*), which is an extension of the TOMCAT 3-D chemical transport model (*79*) to simulate global aerosol containing sulfate (SU), sea salt (SS), black carbon (BC) and organic carbon (OC) for the year 2008. Large-scale transport and meteorology are specified from 6-hourly European Centre for Medium-Range Weather Forecasts (ECMWF) analyses. The horizontal resolution is $2.8°$ by $2.8°$ with 31 vertical levels between the surface and $10\,\mathrm{hPa}$. This low spatial resolution is necessary due to the computationally demanding treatment of the aerosol microphysics.

The particle size distribution is represented using a two-moment sectional (bin) scheme. Two externally mixed distributions are each described with 20 sections spanning dry diameters from $3\,\mathrm{nm}$ to $10\,\mu\mathrm{m}$. The non-hydrophilic distribution, containing only OC and BC, represents freshly emitted primary carbonaceous aerosol (soot) and is not wet scavenged. The hydrophilic distribution contains SU, SS, BC and OC and is wet scavenged. Non-hydrophilic particles are converted to hydrophilic particles through condensation of H_2SO_4 and secondary organic vapors, typically on the timescale of hours to a day. Dust is not included in this particular version of the model because we have previously shown it has an insignificant effect on total particle concentrations, which are the main focus of this study (*80*).

The microphysical processes in the model include nucleation, coagulation, condensation of gas-phase species, in-cloud and below-cloud aerosol scavenging and deposition, dry deposition and cloud processing.

12   Modeled emissions and concentrations

Oceanic DMS emissions were calculated using the ocean surface DMS concentration database of Kettle and Andreae (*81*) and the sea-to-air transfer velocity of Nightingale *et al* (*82*). Volcanic SO_2 emissions from continuously erupting volcanoes and anthropogenic SO_2 from Ref. (*83*) are included. Emissions of biogenic terpenes are from the Global Emissions Inventory Activity (GEIA) inventory based on Guenther et al. (1995) (*84*). Anthropogenic emissions of SO_2 and carbonaceous aerosol from wildfires, biofuel, fossil fuel and volcanoes are based on the Aerosol Inter Comparison Project (AeroCom) emission inventories for the year 2000 (*85*). Elemental (black) and organic primary organic carbon are emitted in log-normal modes which have diameters specified in Table S3. Emissions of sea salt were calculated using the scheme of Martensson *et al.* (*86*) for sizes below $2\,\mu$m and Monahan *et al.* (*87*) above $2\,\mu$m. The overall sea spray flux of approximately $1300\,\mathrm{TgNaClyr^{-1}}$ is much lower than the AeroCom and IPCC values in Ref. (*85*) of $7925\,\mathrm{TgNaClyr^{-1}}$ and $3340\,\mathrm{TgNaClyr^{-1}}$ respectively (though well within uncertainties, which are quoted as 80% in the latter study). The AeroCom value is based on the Gong parametrization (*88*), which does not account for ultrafine sea spray emissions while the Martensson parametrization we use here does (see Fig. 7 of Ref. (*89*) for a much more recent comparison of parametrizations with observations). The overall mass flux may be underestimated by the Martensson parametrization, but this is unimportant as the mass flux is dominated by small numbers of coarse mode particles, and so will not strongly affect CCN numbers, condensation sinks or radiative forcing. On the other hand, accounting for ultrafine particle numbers correctly is critical to accurately calculate the fraction of CCN that originate from nucleation.

Concentrations of the oxidants OH, O_3, H_2O_2, NO_3 and HO_2 were specified using 6-hourly monthly mean 3-D concentrations from a TOMCAT simulation with detailed tropospheric chemistry (*79*). During each 6-hour transport step of the model, concentrations of H_2O_2 are depleted through the aqueous phase reaction with SO_2 and replenished through the reaction $2HO_2 \rightarrow H_2O_2 + O_2$ as described in Ref. (*13*).

The gaseous sulfuric acid that participates in nucleation is produced from a simplified sulfur cycle scheme including the reaction of SO_2 with OH, reactions of DMS and reactions of MSA, while H_2O_2 and O_3 produce sulfate via aqueous phase processing in cloud droplets. Primary sulfate is also emitted in the model as a log-normal mode with diameter $60\,$nm for road and domestic emissions, $150\,$nm for industrial emissions and $1500\,$nm for shipping emissions. This

mode is then mapped to the model size bins. The flux is set to account for 2.5% of the SO_2 emissions. Secondary organic aerosol (SOA) is produced from biogenic terpenes. The terpenes react with OH, O_3 and NO_3 (90, 91) with rates equal to that of alpha-pinene. A fixed 13% of all three reaction products form a first-stage oxidation product that condenses with zero vapor pressure onto existing aerosol (92). This SOA is added to the hydrophilic aerosol distribution and lumped with the OC component from primary sources. The OH also reacts with monoterpenes (MT) to create BioOxOrg for organic nucleation. The concentration of BioOxOrg in the model is given by (24)

$$[\text{BioOxOrg}] = \frac{k[\text{MT}][\text{OH}]}{CS} \tag{3}$$

where $k = 1.2 \times 10^{-11} \exp{(444/T)} \, \text{cm}^{-3}\text{s}^{-1}$ (63) and CS is the condensation sink in s^{-1} calculated from the number of particles in the model and their size, assuming that the condensing vapor is organic. The yield of BioOxOrg is not measured directly, but is a multiplicative component of the prefactor of the organic nucleation rate.

Ammonia emissions are taken from the EDGAR 2.0 inventory (51). The emissions are categorized as originating from fossil fuel use, biofuel combustion, industry, synthetic fertilizers, crops, domestic animals, humans, wild animals, soils under natural vegetation and oceans. All of the above categories are used in present-day simulations, but only the last three in pre-industrial simulations. Gas phase ammonia concentrations are controlled partly by dissolution into aerosol particles and partly by removal in precipitation. As the dissolution process is computationally expensive to model, the gas phase ammonia concentration is determined in the faster GLOMAP-mode aerosol model (93) and is then read into the sectional model as a 3-D time-dependent field with daily time resolution. The dissolution solver, described in a discussion paper (94) now in press in Geoscientific Model Development, models the partitioning of NH_3 and HNO_3 into the aerosol liquid phase, including their chemical interaction with non-volatile sea salt and sulfuric acid. The aerosols are size-resolved. A hybrid of dynamic and equilibrium approaches is adopted, where the dynamic approach models the kinetic interaction of the various acids and bases during the dissolution process, while the equilibrium approach is driven only by the steady-state concentrations of these species. The dissolution solver accounts for the ionic species HSO_4^-, SO_4^{2-}, Cl^-, NO_3^-, Na^+, NH_4^+, and H^+ and the gas phase species HNO_3 and NH_3. Parameterizations developed in Ref. (95) are used to obtain the liquid water contents and activity coefficients.

The simulated atmospheric concentrations of H_2SO_4, NH_3 and organic molecules that participate in nucleation are shown in Figs. S10 and S11. The impact of uncertainties in sulfuric acid and organic concentrations in the very similar GLOMAP-mode aerosol model are documented elsewhere (47). Atmospheric ammonia is difficult to measure due to the high variability in ambient concentrations from order $0.01 \, \text{pptv}$ to $500 \, \text{ppbv}$ near sources (96). The low de-

tection limits of order 1 pptv possible during CLOUD chamber measurements are difficult to achieve in field observations (*97*). However, the IASI satellite (*98*) has measured global column integrated ammonia concentrations. While no quantitative comparison has yet been performed, our simulated ammonia mixing ratios appear to have similar spatial variation to the satellite observations plotted in Refs. (*99*) and (*100*).

13   Ion concentrations for the parameterization of inorganic nucleation rates

The ionization rate due to galactic cosmic rays (GCRs) is calculated in GLOMAP using the lookup tables of Ref. (*101*), which include the effect of the sun's magnetic field on the GCR power spectrum (heliospheric modulation potential) for each month. The ionization rate is shown in Fig. S12. The minimum momentum per unit charge required for a given GCR to overcome the Earth's magnetic field and penetrate to the Earth's surface at a particular longitude and latitude (geomagnetic cut-off rigidity) is calculated from the International Geomagnetic Reference Field (IGRF11) coefficients using the method of Fraser-Smith (*102*). The probability of GCRs interacting with the air and generating ions depends on the atmospheric depth, which is a linear function of atmospheric pressure. Ionization due to radon is included based on a look-up table from Ref. (*103*). At ground level over land, it is usually a larger source of ions than GCRs, and it can still lead to ion pair production rates of $1 - 2\,\mathrm{cm}^{-3}\mathrm{s}^{-1}$ at $4\,\mathrm{km}$ altitude. Perturbations to ion concentrations due to meteorology (see, for example, Refs. (*104, 105*)) are not considered.

The modulation of the GCR flux over the solar cycle is simulated by scaling the heliospheric modulation potential at solar minimum by a factor 3.56, which is equivalent to the ratio of the 2008 mean value to the value of the 20-year solar maximum (*101*). The reference simulations take place during the solar minimum of 2008. Since the ion concentration is not used in the organic simulations (the representation of ion-induced organic nucleation is described in Sect. 15), only the inorganic component of nucleation is perturbed by this modulation. However, the enhancement of ternary organic nucleation when the beam is on compared to the enhancement due to ground-level GCRs was measured to be less important than for inorganic nucleation (*24*), and the ion concentrations are lower at low altitudes where the organic nucleation is most important. Therefore this omission is unlikely to introduce significant error.

14 Modeled nucleation rates

Parameterized nucleation rates at $1.7\,\mathrm{nm}$ diameter from the inorganic and organic CLOUD results are included in the model throughout the atmosphere. The effective particle formation rate at $3\,\mathrm{nm}$ diameter is then calculated using the approach of Kerminen and Kulmala (*68*) assuming a growth rate that depends on the condensation of sulfuric acid and low volatility organic vapors. The condensation sink used assumes the diffusion characteristics of sulfuric acid. Sulfuric acid and ion production rates are evaluated every 30 minutes and modified every 3 minutes to account for losses to condensation, temperature data has a 30 minute time resolution, and $[\mathrm{NH_3}]$ values are daily means. The ion concentrations are calculated from ionization rates as described in Sect. 8. The recombination and loss rates in the ion balance calculation are calculated under local atmospheric conditions of temperature, pressure and aerosol surface area. The inorganic fraction of nucleation is shown at two altitudes for the pre-industrial and present day in Fig. S13. For comparison, simulations are also performed with the binary nucleation mechanism of Kulmala (*106*) together with organic nucleation according to Ref. (*24*), with all other aspects of the model kept the same. This binary nucleation mechanism is based on classical nucleation theory, and should not be confused with the binary neutral nucleation pathway we have determined experimentally in the CLOUD chamber; the comparison with aircraft measurements described later shows that the extrapolated theoretical binary rate from Ref. (*106*) produces far more particles than the rate we determine in this study.

15 Organic ion-induced nucleation

For nucleation involving organic molecules, there is insufficient data to determine the nucleation rate as a function of the ion concentration. However, some measurements of the enhancement of the nucleation rates due to ions do exist (*24*), and these are used to provide an indication of the ion-induced fraction of organic nucleation in the atmosphere. Based on Fig. 1D of Ref. (*24*), we assume that nucleation is 60% ion-induced when the organic nucleation rate is less than $0.1\,\mathrm{cm^{-3}s^{-1}}$, 44% ion induced if it is between 0.1 and $1\,\mathrm{cm^{-3}s^{-1}}$, 28% ion-induced if it is between 1 and $10\,\mathrm{cm^{-3}s^{-1}}$, and zero otherwise. Overall, if the organic nucleation is independent of temperature, approximately 25% of organically nucleated new particles are likely to be formed via ion-induced nucleation. This ion-induced fraction may depend strongly on ambient sulfuric acid concentrations, the possible interaction of ammonia with organic molecules, which was not studied, and on the characteristics of the nucleating organic molecules, which were derived from pinanediol in Ref. (*24*) but which derive from terpenes in the atmosphere. Our quantum chemistry simulations for the temperature dependence of J_{org} assume that the ion-induced fraction of the nucleation rate is only weakly temperature-dependent while the neutral

fraction depends strongly on temperature, so within this model there is a significant yet uncertain variation in these fractions with temperature. In the main text, we calculate that ion-induced nucleation produces more particles than neutral nucleation in 67% of the troposphere. This is based on monthly averages of the ion-induced fractions of formation rates.

16 Pre-industrial simulations, modeled CCN and radiative forcing

Simulations of pre-industrial conditions are performed with anthropogenic sources of ammonia and SO_2 removed from the model, and present-day black carbon and primary organic matter emissions from fossil and bio-fuel combustion replaced with estimates of pre-industrial emissions (*85*). All other aspects of the model, including the 2008 meteorology, remain identical. To determine the radiative effect of anthropogenic ammonia, the present-day simulation is repeated using only pre-industrial ammonia concentrations. As the ammonia concentrations are read into the model from a modal model run (see Sect. 12), only the effects of ammonia on nucleation are accounted for in this radiative calculation.

In both pre-industrial and present-day simulations, newly nucleated particles grow to CCN size via irreversible condensation of sulfuric acid and organic compounds formed via the oxidation of monoterpenes as described in Sect. 12. Uncertainties due to the poorly constrained concentrations of condensable organic material are studied in Sect. 19. To determine the fraction of CCN due to nucleation and compare it to that due to primary emissions, the concentration of CCN at 0.2% is calculated. This is to facilitate comparison with the dedicated study in Ref. (*4*). Elsewhere in this study we quote concentrations of soluble particles of at least $70\,\mathrm{nm}$ diameter, as this is the simplest proxy for CCN: no assumptions about critical supersaturation or hygroscopicity are required. Here, the critical diameter for activation at 0.2% water vapor supersaturation is determined following Refs. (*107*) and (*108*), assuming hygroscopicity parameters of 0.61 for sulfate (assuming ammonium sulfate), 1.28 for sea salt, 0 for black carbon and 0.1 for primary and secondary organic matter.

The fraction of $70\,\mathrm{nm}$ particles in the hygroscopic distribution at cloud level (460-1100m altitude) from nucleation is calculated to be 46%, while the fraction of CCN at 0.2% from nucleation is 43%. The difference is likely because some particles with high organic carbon content are counted as hygroscopic but have low CCN activity. We note that in our simulations all particles are assumed to be internally mixed during activation, even though we do also model the ageing of insoluble particles as sulfuric acid and secondary organic material condense. On land, at cloud level 32% of CCN at 0.2% come from nucleation while over the ocean 51%. The fraction of all particles greater than 3nm in diameter from nucleation is 94% globally (below

$15\,\text{km}$ altitude) and 73% at cloud level. These findings are broadly in agreement with Ref. (*4*).

The same hygroscopicities are used to calculate the cloud droplet number concentrations using the parameterization of Refs. (*109–111*), and hence estimate the radiative forcing over the industrial period. The parameterization models the activation of the particle population within an ascending adiabatic parcel, employing a 'population splitting' concept. Droplets are implicitly categorized as those which continue to grow rapidly following activation beyond their critical diameter, and those which do not. This classification is important to determine the correct droplet size and hence the maximum supersaturation in the cloud and the number of particles that will activate. The supersaturation reaches a maximum when its rate of increase due to parcel cooling becomes equal to its rate of decrease due to depletion of the water vapor by droplets. The population splitting algorithm is applied repeatedly to solve an equation for the maximum supersaturation via a bisection method. Updraft velocities are assumed to be $0.15\,\text{ms}^{-1}$ over sea and $0.3\,\text{ms}^{-1}$ over land. The parameterization is validated against a numerical cloud parcel model in Ref. (*111*).

The radiative forcing is determined from the cloud droplet number concentrations using the Edwards and Slingo radiative transfer model (*112*) following methods described in Ref. (*113*). In the control simulation, the model uses a monthly mean climatology based on ECMWF re-analysis data, together with cloud and surface albedo fields from the ISCCP-D2 archive (*114*) for the year 2000. Calculations of cloud albedo changes between control and perturbed simulations are determined from the changes in cloud effective radius driven by the difference in cloud droplet number concentrations as in Ref. (*115*). The first Aerosol Indirect Effect is calculated by comparing all-sky net radiative fluxes at the top of the atmosphere across the six short-wave and nine long-wave bands.

17 The role of amines

Amines are likely to be important to nucleation in some areas of the planetary boundary layer over land. Amine concentrations are modelled in Refs. (*116*) and (*40*) and we follow a similar strategy here to estimate their concentrations. We then use data from the CLOUD chamber published in Ref. (*23*) to produce a first estimate of the contribution of amines to nucleation rates. We use the faster GLOMAP-mode aerosol model for technical reasons.

We produced an amine emissions inventory by taking the EDGAR ammonia emissions categories (*51*) and using Ge *et al.* (*117*) to estimate a factor to scale down each source of ammonia emissions to get realistic emissions of amines. We assume amine emissions are the sum of 0.66% of ammonia emissions from wild and domestic animals, 0.45% of ammonia emissions from oceans, and 1% of ammonia emissions from biofuel combustion. Amine emissions from the other ammonia categories of crops, fertilizers, fossil fuels, industry, soils under natural veg-

etation and humans are not known so are assumed to be zero.

We then ran simulations with a tracer for a single amine, which reacts with OH with the rate for dimethylamine and is lost to aerosol irreversibly with a sticking coefficient of 0.03, the upper value used in Ref. (*116*). It is also removed via dry and wet deposition. The concentrations that result are comparable to Ref. (*116*) close to the surface. We find amines do not live long enough to be present in the free troposphere at significant concentrations, which is consistent with literature.

We neglected the diurnal cycle of amine emissions, which is considered in detail in Ref. (*40*), as its effect is likely to be small compared to the overall uncertainty on emissions and nucleation rates. The resulting annual mean concentration of our amine, averaged between the surface and 500 m altitude, is shown in Fig. S14A.

We parameterize nucleation rates of dimethylamine (DMA) and sulfuric acid measured at the CERN CLOUD chamber and presented in Ref. (*23*). Assuming all amines nucleate at the same rate as DMA, we find three parameterizations would fit the chamber data in Ref. (*23*) acceptably well. The median nucleation rate of the three is given by

$$J = k \frac{[\text{DMA}]}{2.5 \times 10^7} [\text{H}_2\text{SO}_4]^{3.7} \tag{4}$$

for $[\text{DMA}] > 2 \times 10^8 \, \text{cm}^{-3}$, and

$$J = k \left(\frac{[\text{DMA}]}{2.5 \times 10^7} \right)^{4.36} [\text{H}_2\text{SO}_4]^{3.7} \tag{5}$$

for $[\text{DMA}] < 2 \times 10^8 \, \text{cm}^{-3}$.

The DMA and H_2SO_4 concentrations are in cm^{-3}; the value of k is 2.08×10^{-25} above $[\text{DMA}] = 2 \times 10^8 \, \text{cm}^{-3}$ and 1.93×10^{-28} below. Since we only use data from Ref. (*23*), the sulfuric acid dependence we obtain is stronger than in Fig. 2 of Ref (*40*).

In this case, we find that nucleation involving amines accounts for around 6% of new particle formation within 500 m of the surface and negligible amounts above. The annual mean nucleation rates due to the amine mechanism, averaged betweent he surface and 500 m altitude, are shown in Fig. S14B. With this model, the nucleation in this altitude range is 84% organic, 6% amine and 10% inorganic (mostly ternary ion-induced). Using the same amine concentrations but different parameterizations of the nucleation rate compatible with the data of Ref. (*23*) we find this fraction could vary between 3% and 27%. When the amine nucleation fraction is 27%, the inorganic fraction is 7% and the organic fraction 66% within approximately 500 m of the surface. We emphasise that this is an extreme scenario, likely to be a realistic upper limit, since DMA is the most effective amine for nucleation so far discovered.

There is a large uncertainty on amine emissions that we did not attempt to investigate further, since this is unlikely to affect the vertical distribution. The amine lifetime will be more strongly

affected by the loss processes. When we adjusted the sticking probability to 0.001, we found the fraction of amine nucleation in the first 500 m of altitude increased from 6% to 10%. As expected the fraction of amine nucleation in the surface layer increases by a smaller amount, from 14% to 17%, as the amines live longer and therefore get higher into the troposphere.

Given that we have probably overestimated nucleation involving amines, since DMA is a more potent nucleating agent than other amines, it seems likely that organics are substantially more important than amines for atmospheric nucleation when considered globally, although amines may well be more important in India, some parts of the US, central Europe and eastern China.

We find that adding amines does not make a large difference to the results for CCN concentrations: the enhancement of nucleation rates and ultrafine particle concentrations due to nucleation involving amines is in areas where primary and secondary aerosol from pollution is already high, and so most nanosized particles will be lost before they can grow to CCN size. Including our baseline amine nucleation mechanism increases global average cloud-level concentrations of 70nm particles by less than 0.1%. Locally, surface-level CCN concentrations do increase by up to 3% in northern India, 1% in Europe, and negligibly elsewhere, as shown in Fig. S14C.

18   Comparison of the global aerosol model with ambient measurements

GLOMAP has been extensively evaluated against observations, and reproduces the observed particle number concentration well in both continental (*118*) and marine regions (*119*). The size distribution over Europe is compared to observations in Refs. (*120*) and (*121*). We redo some of these comparisons to check the model performance remains good when compared to observations.

An extensive dataset of total particle number concentrations observed at 35 worldwide sites is used to evaluate the present nucleation model and quantify the primary and secondary sources of particle number (*43*) (Fig. S15). Zugspitze is omitted from the figure compared with Ref. (*43*) to allow the sites to be plotted on a 7×5 grid. Measurements at these sites were made with CPCs, SMPS's, diffusion aerosol spectroscopes, or differential mobility particle sizers, mostly between 1995 and 2008. Where datasets exist for multiple years, averages are calculated for each month.

The model bias relative to observations when different components of nucleation are included is detailed in Table S4. Overall, the model underestimates total particle number concentrations by 25%, for reasons discussed below. The cut-off sizes of the instruments measuring at

each site, below which the particles were not counted, ranges from 3 to 14 nm and is also given in the table.

Binary neutral nucleation of sulfuric acid and water alone clearly cannot explain the observed particle concentrations. Most of the sites are in the Northern Hemisphere (NH), so Fig. S15 shows that organic nucleation almost always dominates during the NH summer while inorganic nucleation is particularly important in winter. The contribution from organic nucleation is more important at low altitude sites such as Hyytiälä, Värriö and Utö while the high mountain top sites such as Nepal or Pico Espejo have greater contributions from inorganic nucleation. The model substantially underestimates observations in some polluted or coastal sites such Po Valley, Point Barrow and Mace Head. This is likely to be due to contributions to nucleation from anthropogenic organic molecules, amines or iodine. There is also a relatively large uncertainty in the emissions of DMS in the model compared to anthropogenic SO_2 emissions. The overestimation of $3 - 14$ nm particle concentrations in summer that is most pronounced at Trinidad Head appears to be due to the organic component of nucleation. This could be due to an overestimation of the mass flux of organic molecules onto newly nucleated particles to grow them to the cut-off size of the CPC. Alternatively, the organic nucleation rate could be overestimated at high summer temperatures, or the terpene emissions could be overestimated there. Overall, Table S4 indicates that particle concentrations are most significantly underestimated in the three Northern Hemisphere winter months, probably due to the omission of some nonvolatile anthropogenic vapors from the model, while they are also slightly underestimated in the three summer months, probably for the same reasons. The underestimation of particle numbers in spring and autumn is less (see, for example, Bondville or Thompson Farm in Fig. S15), leading to a smaller bias over the whole year.

The performance of the model at altitudes of up to 12 km above the surface is evaluated by comparing its predictions for 3 nm particle concentrations with observations. The observations were made during eight aircraft campaigns: ACE1 (October-December 1995), PEM Tropics A (August-September 1996), INDOEX (February-March 1999), PEM Tropics B (March-April 1999), INTEX-A (July-August 2004), PASE (August-September 2007), ARCTAS (March-July 2008) and VOCALS (October-November 2008). Most of these sample ocean regions, the main exception being INTEX-A, which was mostly over the USA. The locations of the measurements are shown in Fig. S16. The particle concentrations were measured with CPCs aboard C-130 (ACE1, INDOEX, PASE, VOCALS), P3B (PEM) or NASA DC-8 or P3-B (PEM, INTEX-A, ARCTAS) aircraft.

The objectives of the earlier campaigns included determining the conditions favourable for nucleation in the marine free troposphere. In ACE1 (*45*) and PEM Tropics (*46*), particle production was found to be particularly enhanced in cloud outflow regions of intermediate to high relative humidity (RH) in the period shortly after midday, especially when condensation sinks

24

were low due to cloud scavenging. Later campaigns placed more emphasis on the roles of relative humidity (INDOEX (*122*)), tropospheric composition over land (INTEX (*123*)), sulfur processing (PASE (*124*)), Arctic atmospheric composition (ARCTAS (*125*)) and linking aerosols, clouds and precipitation in the south-eastern Pacific (VOCALS (*126*)).

The one-minute-averaged CPC concentrations from each campaign are compared with model output from dedicated simulations of the particle concentrations for the same days as the observations were recorded. The modeled particle concentrations are converted to values at standard temperature and pressure (300 K, 1000 hPa). The daily mean particle concentrations predicted by the model are determined for the latitude and longitude of each observation by interpolating within model grid boxes in all three dimensions. As the simulations are performed over the time period of each campaign, the meteorology data from ECMWF will match the weather systems observed by the aircraft. However, the model time resolution of one day and spatial resolution of $2.8°$ in latitude and longitude and a few hundred metres in altitude limits the precision of the comparison.

The data points are compared in Fig. 3 of the main text. In all, there are 65,856, so many overlap with others and cannot be seen. Therefore, the density of different concentrations as a function of altitude is also plotted in Fig. S17. The median particle concentrations and 10%-90% ranges are shown for each campaign and the normalized mean bias of the model is compared with that of a model run with only binary neutral nucleation, and a model run with the nucleation rate parameterization used in Ref. (*24*), re-implemented in the sectional aerosol model, in Table S5.

As is also evident from the comparison of the model with observations at surface sites, binary neutral nucleation cannot explain particle concentrations. The model with nucleation from Ref. (*24*), which uses Ref. (*106*) to parameterize sulfuric acid nucleation in the free troposphere, tends to over-predict particle concentrations. The altitude dependence of the predictions suggests that this is due to inorganic nucleation. Our model slightly under-predicts particle concentrations on average, with relatively large variations in its agreement with data between campaigns (Table S5) and with altitude (Fig. S17). The general trend for higher particle concentrations at higher altitude over the ocean, and for a more complex structure over land (INTEX) is reproduced relatively well.

In ACE1, PEM-A, ARCTAS and VOCALS there is quite good agreement between model and observations on average, though in PEM-A the variance in the model is greater than that in the data at low altitude, perhaps due to there being insufficient resolution to fully capture sub-grid subsidence processes. In PEM-B the model significantly over-predicts particle concentrations at high altitude, as does the parameterization of Ref. (*106*). The high-altitude data were taken at latitudes in the range $25 - 40°$N, while the low-altitude observations are mostly in the range $0 - 20°$N. This is consistent with the finding in Ref. (*127*) that Aitken mode particle

concentrations are under-predicted in Southern Hemisphere mid-latitudes and over-predicted in the Northern.

The particle concentrations observed in INDOEX come from fewer flights. They show a structure at around 2 km altitude which is blurred in the model by the low resolution to the point where it cannot be seen in the profiled density function (Fig. S17D), but direct comparison of the modeled concentrations for this campaign (not shown) indicates it is still present to some extent.

The particle concentration at very high altitude is underestimated in INTEX-A, and the altitude variation is not as pronounced as in the observations. The reasons for this are not clear. Concentrations are also underestimated at all altitudes above the boundary layer when compared to the PASE observations. Literature relating to this campaign indicates the possible explanation that dry deposition velocities of SO_2 measured via the eddy covariance technique could be lower than those in our model (*124*). Speculatively, this could lead to the model underestimating sulfate, but it may also lead to lower condensation sinks and thus the consequences for nucleation are not clear.

Ref. (*128*) provides the numbers of nucleation events observed each month in 2008-2009 at various field observation sites. We compare our model results with their data for April-July 2008 at 8 sites: Pallas, Hyytiälä, Mace Head, Melpitz, Hohenpeissenberg, Jungfraujoch, Vavihill and Finokalia. We output modelled size distributions at these sites with hourly time resolution, and, following Ref. (*129*), we count events in which the $dN/d \log D_p$ value in the mean of three size bins around $10 \, \text{nm}$ exceeds $3000 \, \text{cm}^{-3}$, and in which the size distribution shows a growing size mode. We note that our size bins are not identical to those used in Ref. (*129*). These criteria are designed to select those events that would probably be distinguishable from experimental backgrounds in observation data, but are necessarily defined subjectively in that looser or tighter thresholds could also be justified, depending on characteristics of aerosols at the site in question.

An example of a modeled size distribution (at Hyytiälä in April 2008) and the results of the comparison of the frequencies of nucleation events are presented in Fig. S18. In total, 350 nucleation events are observed and 272 are counted in the model output. The model is in good agreement with observations (within, or close to, a factor of two where statistically significant numbers of events occur) except at Melpitz, where many more nucleation events are observed than the model predicts. This is likely due to a failure to resolve strong local sources of vapors at this site. In general more nucleation events are predicted at the Finnish boreal sites Hyytiälä and Pallas than observations, and fewer in the more polluted European regions. The excess in Finland is likely due to an overestimate of terpene emissions there while the reduced number of events in polluted Europe could be due to nucleation events triggered by anthropogenic organic compounds or amines which we do not include in our baseline model. The time of day of the nucleation events is well captured (see Fig. S18A for Hyyälä). A comparison of a different

model with the same observations is given in Ref. (*130*). Overall, our model performs in line with expectations.

While limited resolution and large uncertainties in emissions continue to result in variable levels of agreement between model and observations, we emphasise that no artificial tuning of the particle concentrations or the growth or loss rates that influence them together with the nucleation rate was used to adjust the model to agree with the observations. Overall, the model results reproduce well both aircraft and surface site observations.

19   Assessment of uncertainties

The uncertainties in the analysis reported here can be split into those which apply to the parameterized nucleation rates and those which apply to the modeled particle concentrations and radiative forcing. The first category contains components from the measured nucleation rates, the gas concentrations, and biases in the fit of the parameterization to the data. The second has many contributions which are studied in detail for a very similar aerosol model in Refs. (*47*) and (*52*). In this category we consider only uncertainties in concentrations of secondary organic molecules produced from terpenes due to terpene emissions and yields, growth rates of freshly nucleated aerosol, and the temperature dependence of the organic nucleation rates. These uncertainties are particularly pertinent to this study and are not studied in Ref. (*47*).

The uncertainties in the measured nucleation rates are associated with the characterization of the particle counters, especially at low temperatures, and the extrapolation of the measured particle formation rate at $3.2\,\mathrm{nm}$ down to the $1.7\,\mathrm{nm}$ diameter. The overall uncertainty in the nucleation rate at $1.7\,\mathrm{nm}$ diameter is estimated to be a factor of 2.5. The effect of increasing modeled inorganic nucleation rates by this factor is a $+2.0\%$ change in the global concentration of $70\,\mathrm{nm}$ particles at cloud base level for March-June inclusive, while decreasing the inorganic nucleation rates leads to a -2.1% change. The time period was selected to be relatively representative of the year. Since the organic nucleation experiments were all conducted at $278\,\mathrm{K}$, the nucleation rates could be determined from a deg-CPC with a lower cut-off size of $2\,\mathrm{nm}$, and therefore the uncertainty due to the correction down to $1.7\,\mathrm{nm}$ is smaller (estimated in Ref. (*24*) as $+58\%/-45\%$). This is small compared with the uncertainty in the measured sulfuric acid concentration, and was therefore not investigated further.

The uncertainty in sulfuric acid concentration for inorganic nucleation rates is $+50\%/-33\%$ (Sect. 5). It is larger for organic nucleation rates ($+100\%/-50\%$) because of possible reactions between pinanediol and sulfuric acid. Therefore we perturb separately the concentrations of sulfuric acid used in both inorganic and organic nucleation rate calculations by a factor 2. Testing organic and inorganic nucleation separately allows us to compare how sensitive the model results (nucleation rates and CCN) are to sulfuric acid in each case. The uncertainty in sulfuric

acid concentrations leads to a change in CCN concentrations of $+3.2\%/-2.9\%$ for inorganic nucleation over March-June. The effect of sulfuric acid concentration uncertainty on organic nucleation is estimated to be $+4.1\%/-3.7\%$ over March-June, with larger regional effects shown in Fig. S19. The uncertainty in the sulfuric acid concentration is slightly larger at low temperature due to increased clustering. To determine an upper bound for the effect on the modeled temperature dependence of nucleation and CCN of these uncertainties, the parameterization of nucleation rates was repeated with the sulfuric acid concentration at $208\,\mathrm{K}$ scaled up by a factor 2 and at $223\,\mathrm{K}$ by a factor 1.5, and the resulting change in cloud-base level CCN for March-June was only -0.2%.

The uncertainty in concentrations of ammonia measured in the CLOUD chamber depends on the concentration, as discussed in Sect. 6. To investigate the sensitivity to these uncertainties, the NH_3 concentrations were set to the highest and lowest values allowed by the experimental error range and the parameterization was re-fitted in the two cases. The result is a small reduction of CCN by 0.8% at low NH_3 concentrations and an increase of 0.4% at high NH_3 concentrations but larger changes to the fractions of nucleation from each pathway detailed in Table S7.

The uncertainty in the functional form of the inorganic parameterization will mostly affect the relative fractions of binary neutral, binary ion-induced, ternary neutral and ternary ion-induced inorganic nucleation rates, and has only small effects on CCN.

The rate of binary neutral nucleation is poorly constrained from below: leaving binary neutral nucleation out of the parameterization still gives good agreement with the nucleation rate data. The parameterization function is chosen conservatively to produce the highest value of binary neutral nucleation permitted by the data. However, this form, which constrains the ratio of binary to ternary nucleation, is verified as correct for the ion-induced case, because ammonia is confirmed to be absent from the nucleating charged clusters. Removing binary neutral nucleation and refitting the parameterization leads to an annual average change in particle concentrations at cloud base level of only -0.1%. As expected, the overall nucleation rates and CCN are insensitive to the details of the parameterization, provided that it agrees well with the CLOUD data. However, there is a more significant change to the contributions of the various nucleation pathways below $15\,\mathrm{km}$ to 0.0% binary neutral, 9% binary ion-induced, 46% ternary neutral, 16% ternary ion-induced and 29% organic. For comparison, the baseline model predicts 2% binary neutral, 10% binary ion-induced, 53% ternary inorganic neutral, 10% ternary inorganic ion-induced and 26% ternary organic nucleation over March-June. The fact that the ternary fractions change, beyond simply subsuming the binary neutral fraction, reflects the change to the rest of the parameterization caused by constraining the binary neutral fraction to zero, and is a further measure of the parameterization uncertainty. The variations to these fractions when (for example) the parameterization is varied to account for the uncertainty in ammonia concen-

trations, or the model is varied to change the quantity of sulfuric acid participating in a given nucleation pathway, are given in Table S7.

When the empirical function used to represent the temperature dependence of each nucleation pathway is replaced with a simpler function, the fractions of the different pathways over March-June change to favour ion-induced nucleation over neutral nucleation: the binary ion-induced fraction of nucleation below $15\,\mathrm{km}$ altitude increases from 9.7% to 15% over March-June and the ternary ion-induced fraction increases from 9.6% to 37.5%. This reflects the uncertainty in the ion-induced contribution to the nucleation rate at low temperatures. With this parameterization, the overall nucleation rate increases compared to the baseline case, and therefore the relative fraction of organic nucleation decreases.

The uncertainties in the organic parameterization are more difficult to quantify. In particular, the use of a proxy, pinanediol, for monoterpenes in Ref. (*24*) leads to an uncertainty in how well the proxy represents the monoterpenes when the results are used in our aerosol model. To attempt to quantify the uncertainties associated with the organic nucleation rates in general terms, we test the effect on CN and CCN of using a completely unrelated parameterization of organic nucleation, derived by Paasonen *et al* from EUCAARI field observation data (*131*) instead of the CLOUD chamber data in Ref. (*24*). In Ref. (*131*), eight possible parameterizations are obtained from the field data. The best agreement with observations is obtained using

$$J = K_{SA1}[\mathrm{H}_2SO_4]^2 + K_{SA2}[\mathrm{H}_2SO_4][org] \tag{6}$$

where $[org]$ is the concentration of vapors required to explain the observed growth rates from $2 - 4\,\mathrm{nm}$. In GLOMAP, we have different growth rates between 2 and $3\,\mathrm{nm}$ and between 3 and $4\,\mathrm{nm}$. These growth rates correspond to different vapor concentrations. Since the parameterization was derived from data taken at Hyytiala, Melpitz and Hohenpeissenberg, we compare the particle numbers predicted by our implementation of the parameterization using the two alternative growth rates with observations at these sites to determine which growth rate should be used. We find that using the growth rate between 3 and $4\,\mathrm{nm}$ gives better agreement, so we use the concentration of the vapors that correspond to this growth rate in the Paasonen nucleation parameterization, Equation 6. We note that this is not the same organic as the BioOxOrg used in our standard organic nucleation mechanism, but rather the organic that condenses onto all particles larger than $3\,\mathrm{nm}$ in diameter (see Sect. 12). In our model, this new parameterization replaces only the organic nucleation rate. Therefore, we introduce only the second term in Equation 6 to the model instead of the mechanism of Ref. (*24*). Since this term is linear in sulfuric acid, this is relatively similar to an activation-type parameterization for nucleation in the boundary layer. The first term in Equation 6 is not used because we still represent inorganic nucleation with the parameterization described in Sect. 8. Making this replacement leads to a global annual mean concentration of particles of at least $3\,\mathrm{nm}$ in diameter 3.5% higher than

29

the simulations using the CLOUD organic parameterization. The global mean change in cloud base-level CCN (annually averaged), as represented by particles greater than $70\,\mathrm{nm}$ in diameter, is $+2.6\%$. Most of the change is concentrated in forested regions. This variation is around half the variation due to possible temperature dependence of the organic nucleation rate.

The changes in CN and CCN when the parameterization from Ref. (*131*) is used are accompanied by a change in the relative importance of organic nucleation compared to inorganic nucleation. Over a full year, the fraction of particles formed via organic nucleation decreases within $15\,\mathrm{km}$ of the surface decrease from 21% to 16% (Table S7). The changes are due to the linear rather than quadratic dependence of the organic nucleation rate on sulfuric acid concentrations. The decrease is mostly at high altitude, since organic concentrations at high altitudes are relatively low and sulfuric acid high. Conversely, nucleation rates increase compared to the baseline model in regions like the Amazon where sulfuric acid concentrations are low. This increase at low altitude causes the slight increase in cloud-level particle concentrations despite the overall tropospheric decrease in the importance of the organic nucleation pathway.

The uncertainty in modeled biogenic terpene emissions in the atmosphere is studied by perturbing terpene concentrations by $-50\%/+100\%$. This leads to a change of $-6.9/+8.9\%$ in global $70\,\mathrm{nm}$ particle concentrations at cloud base level over March-June, with slightly larger local changes than those seen in Fig. S19. This period of the year is likely to be the most sensitive to organic emissions. The uncertainty in the growth rates of aerosol from $1.7\,\mathrm{nm}$ to $3\,\mathrm{nm}$ due to the condensation of volatile organic compounds is also studied by changing the growth rates by $-50\%/+50\%$. This leads to a change of $-1.2/+0.6\%$ in cloud base level CCN over March-June.

The uncertainty in modeled $[\mathrm{NH_3}]$ is likely dominated by loss processes during long-range transport, especially wet removal and scavenging by existing acidic aerosol. For $\mathrm{H_2SO_4}$, the main uncertainty above the planetary boundary layer (PBL) is likely to be vertical transport and removal of the precursor gas $\mathrm{SO_2}$. Concentrations of $\mathrm{SO_2}$ in GLOMAP are typically simulated within a factor 2-3 of observations above the PBL (*13*). Accounting for additional uncertainty in oxidants and loss of $\mathrm{H_2SO_4}$ to existing aerosol, we estimate the total uncertainty in $[\mathrm{H_2SO_4}]$ to be less than a factor 10.

20 Model sensitivity to the temperature dependence of organic nucleation

The lack of experimental data on the temperature dependence of ternary organic nucleation introduces additional uncertainty on the overall fractions of organic and inorganic nucleation in the atmosphere. Introducing a temperature dependence based on quantum chemistry simula-

tions of MBTCA to the model leads to an overall increase in the fraction of organic nucleation below $15\,\mathrm{km}$ altitude from 21% to 69%, resulting from an increase in organic nucleation at high altitude. The fraction of particles formed by organic ion-induced nucleation decreases from 25% to 2.5% since the temperature dependence is applied only to neutral nucleation: ion-induced nucleation is assumed to be independent of temperature. Therefore the maximum decrease in total nucleation rate at high temperatures is limited because the ion-induced nucleation rate is unaffected.

However, as mentioned in the main text and Sect. 10, this temperature dependence is almost certainly too strong, as organic reactions that produce low-volatility compounds slow down at low temperatures. Therefore we tried a weaker dependence, which has no physical basis but lies roughly between the baseline case (no temperature dependence) and the MBTCA case. This leads to a fraction of organic nucleation of 43%.

We note that over the range of altitudes in which aerosols have the strongest effect on clouds, between the surface and around $1100\,\mathrm{m}$, the relative roles of the different nucleation pathways are different to the roles in the whole troposphere. In this interval, 74% of particles originate from organic nucleation in our standard parameterization. Introducing even the extreme temperature dependence from MBTCA only changes this to 82% on average.

Annually averaged, a reduction in $70\,\mathrm{nm}$ particle concentrations at cloud base level of 0.1% in the Northern Hemisphere and of 1.1% in the Southern Hemisphere is predicted when the temperature dependence for MBTCA neutral nucleation is introduced for organic nucleation. The global average reduction is -0.4%. Local changes, however, are higher. The effect on nucleated particles above 3 nm diameter at the surface and at high altitude is substantially larger, as shown in Fig. S20. The figure shows that the increase in nucleation at high altitude leads to a large increase in particle concentrations. This translates to a small reduction in CCN concentrations due to increased competition for condensable vapor to grow the particles to CCN size. At the surface, the warmer temperatures in the tropics lead to a reduction in particle numbers while the colder temperatures at extreme latitudes result in increased nucleation.

We also studied the effect of a projected mean temperature increase of $2.2\,\mathrm{K}$ over the next 100 years. The effect on CCN at cloud base level is shown in Fig. S21 for two cases: when organic nucleation does not depend on temperature, and when it depends on temperature as estimated for MBTCA. Only a small effect is seen. This is expected since $2.2\,\mathrm{K}$ is small compared with the variation in temperature across the troposphere that drives the changes in Fig. S20. We conclude that only a weak positive feedback on climate is expected due to the suppression of CCN formation from nucleation as temperatures increase.
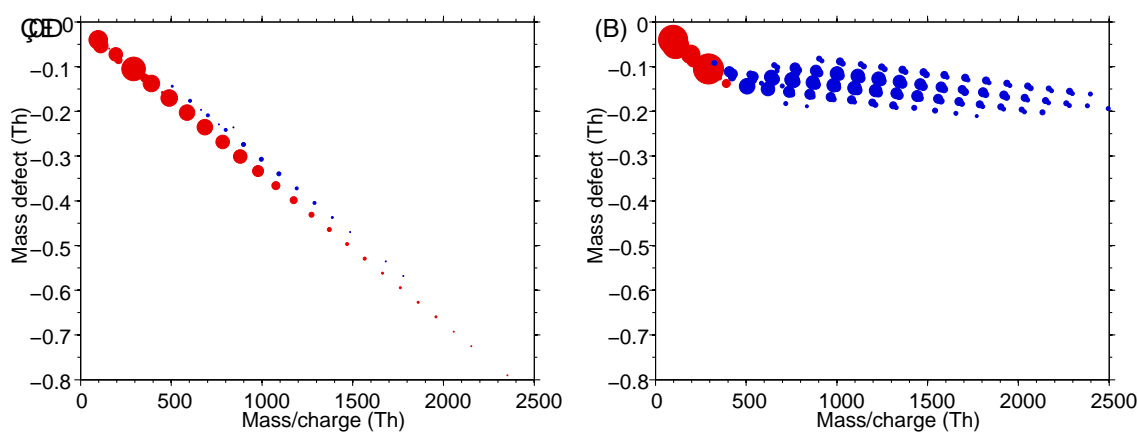
Figure S1: Mass defect plots from the APi-TOF for nucleation experiments at $278\,\mathrm{K}$, with (A) $4.4 \times 10^8\,\mathrm{cm}^{-3}$ ($17\,\mathrm{pptv}$) sulfuric acid and no added ammonia and (B) $7.5 \times 10^7\,\mathrm{cm}^{-3}$ ($3\,\mathrm{pptv}$) sulfuric acid and approximately $35\,\mathrm{pptv}$ ammonia. Red dots represent pure charged sulfuric acid clusters while blue dots represent clusters containing sulfuric acid and ammonia. Each point corresponds to a distinct molecular composition of sulfuric acid and ammonia, with the area proportional to counting rate. The background ammonia mixing ratio in the left plot is estimated to be $2\,\mathrm{pptv}$ (*34*).
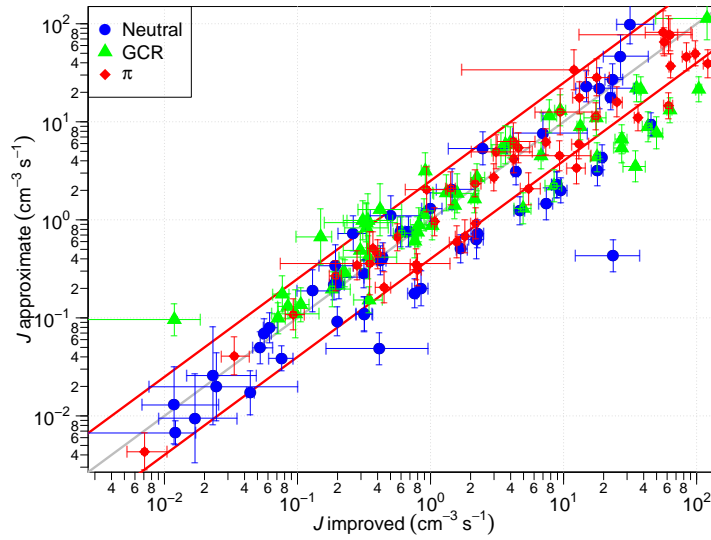
Figure S2: Comparison of the nucleation rates J calculated with the linear growth approximation and those calculated with the multi-step approach of Kürten *et al* (*70*). Almost all data points are within a factor of four of the 1:1 line shown in grey, and 73% are within the factor of 2.5 used as the uncertainty on J (red lines). The nucleation rates are categorized as neutral when the clearing field is switched on to remove ions from the chamber, GCR when the clearing field is off and π when the pion beam from the CERN Proton Synchrotron is on. Uncertainties in individual nucleation rates are determined by combining the uncertainties in particle concentrations, growth rates and loss processes.
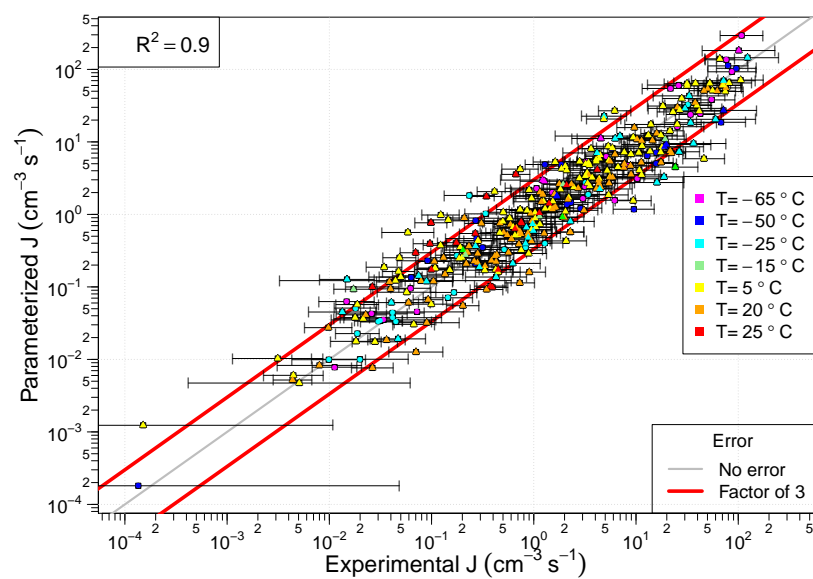
Figure S3: Nucleation rates: parametrized values plotted against fitted values, for the evaluation of the quality of the optimization.
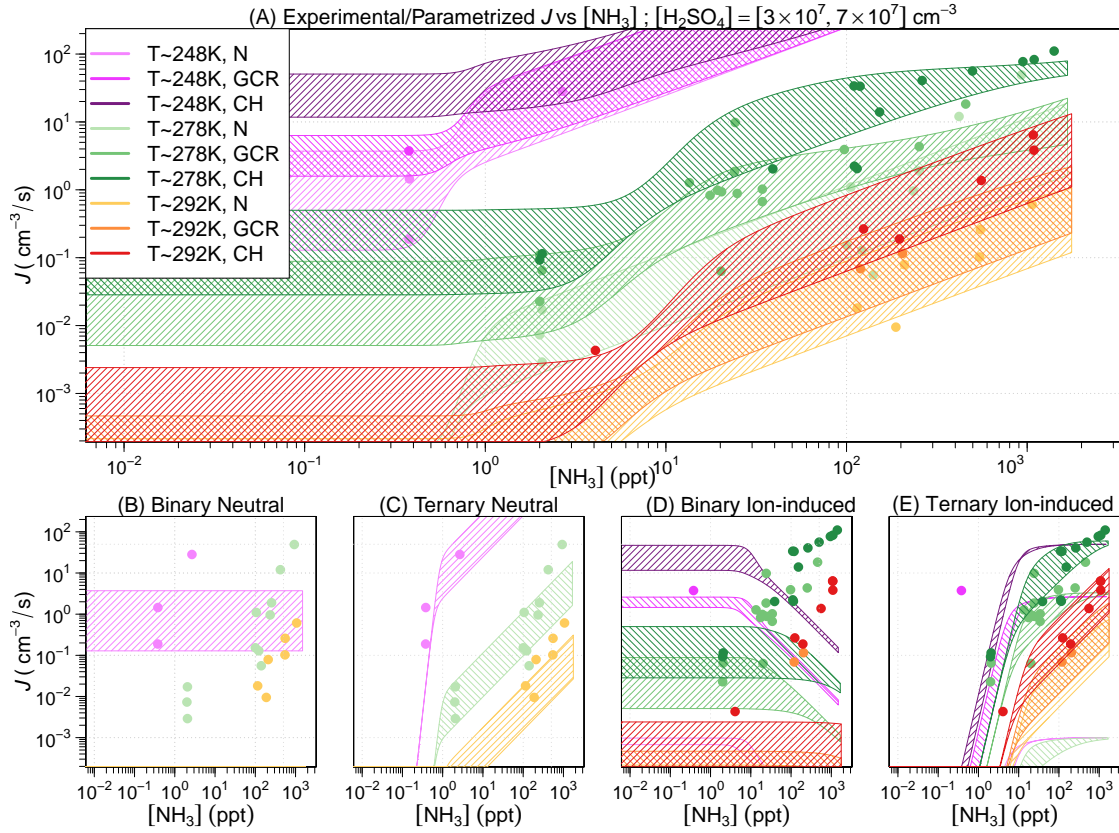
Figure S4: Dependence of $f([\text{NH}_3], [\text{H}_2\text{SO}_4])$ on $[\text{NH}_3]$. (A): Nucleation rates in a narrow range of $[\text{H}_2\text{SO}_4]$ as a function of $[\text{NH}_3]$. The shaded regions show the range of J values predicted by the parameterization corresponding to the highest and lowest allowed H_2SO_4 concentrations. (B) and (C): Measurements of J made in neutral conditions compared with the binary and ternary neutral components of the parameterization. The green and orange data points are not explained by binary nucleation, but are primarily ternary. The plot shows this as the green and orange bands for binary neutral nucleation in (B) lie below the x axis and do not describe the green and orange data, while the same data points plotted in (C) are explained by the bands for ternary neutral nucleation, which are shown in (C) but not in (B). The pink data points have significant binary and ternary contributions. The change of slope of the parameterization at 0.5-5 pptv corresponds to the assumption based on APi-TOF measurements that ammonia readily evaporates from the smallest clusters and therefore has a saturation-like behaviour (see text). (D) and (E): Ion-induced contributions to the nucleation. The data points contain contributions from both neutral and ion-induced nucleation. Dark colours indicate data taken with the beam on (high ion production rates) and lighter colours indicate GCR conditions. The ion-induced components of the parameterization for GCR and beam conditions are shown. The green, orange and red data are explained by ternary ion-induced nucleation, while the single pink data point is binary ion-induced and cannot be explained by ternary ion-induced nucleation as the $[\text{NH}_3]$ is too low. When read with subfigures (A) and (B) it can be inferred that the green data points are mostly explained by a sum of ternary neutral and ternary ion-induced nucleation, the dark pink data points by binary ion-induced nucleation, and the orange and red data points are almost entirely the result of ternary ion-induced nucleation.
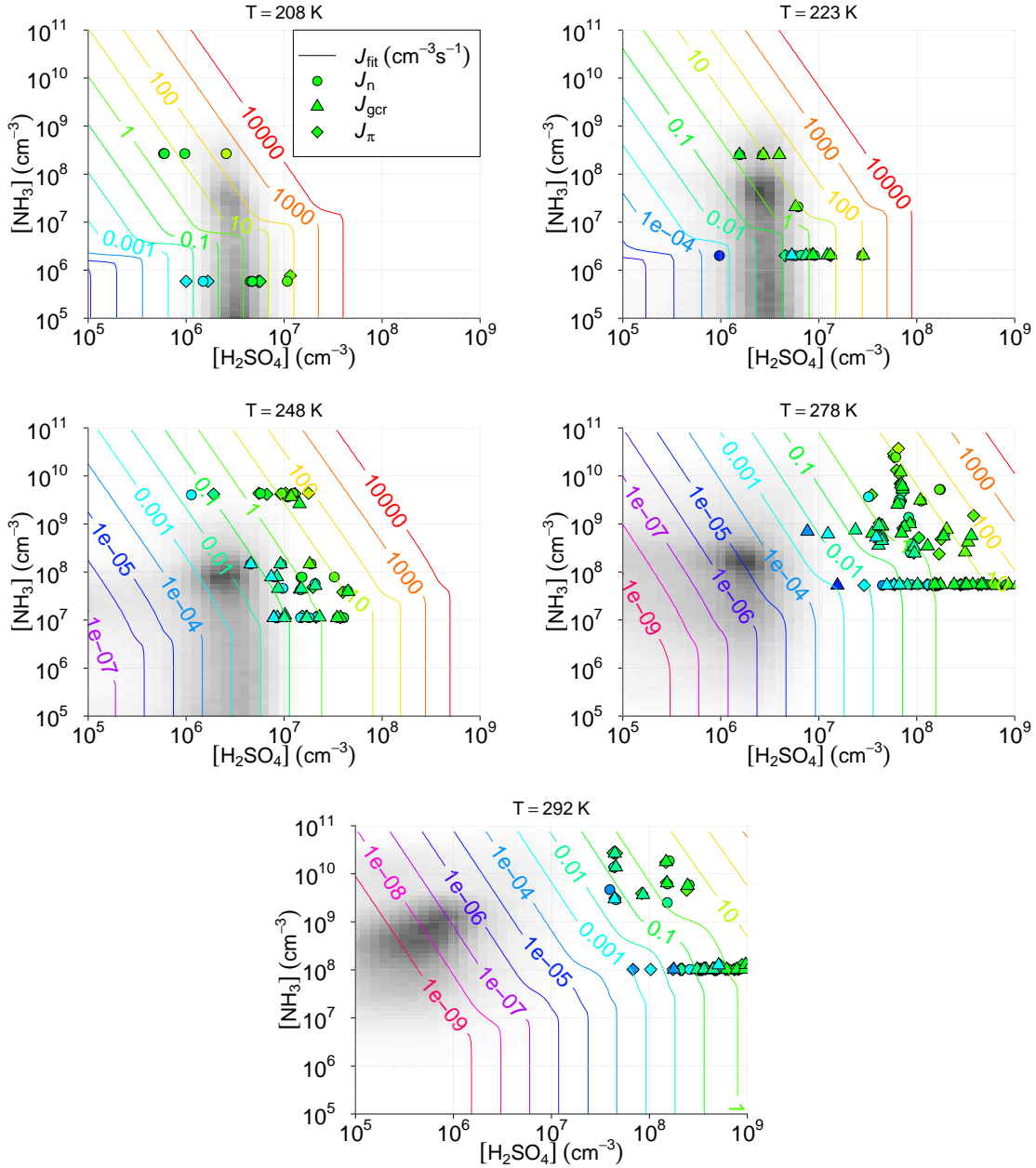
Figure S5: Nucleation rate parameterization dependence on ammonia and sulfuric acid concentrations, shown with the CLOUD measurements (green and blue data points) and the distribution of atmospheric concentrations for context. The parameterization is represented by colored lines, calculated assuming the ground-level GCR ionization level of 1.8 ion pairs per cm^{-3} at 298 K. The color scale of the data points indicates nucleation rate and is given by that of the parameterization lines. The parameterization and CLOUD data are superposed on a density function of the daily mean sulfuric acid and ammonia concentrations in global model grid boxes during a period in 2008 between 10 March and 13 July (the dates of the ARCTAS campaign). The grid-box mean sulfuric acid concentrations are multiplied by two to approximate the fact that they are zero at night. The density function samples from grid boxes at all altitudes of the model, but only at temperatures within approximately $\pm 10\,\mathrm{K}$ of the temperature shown in each plot.
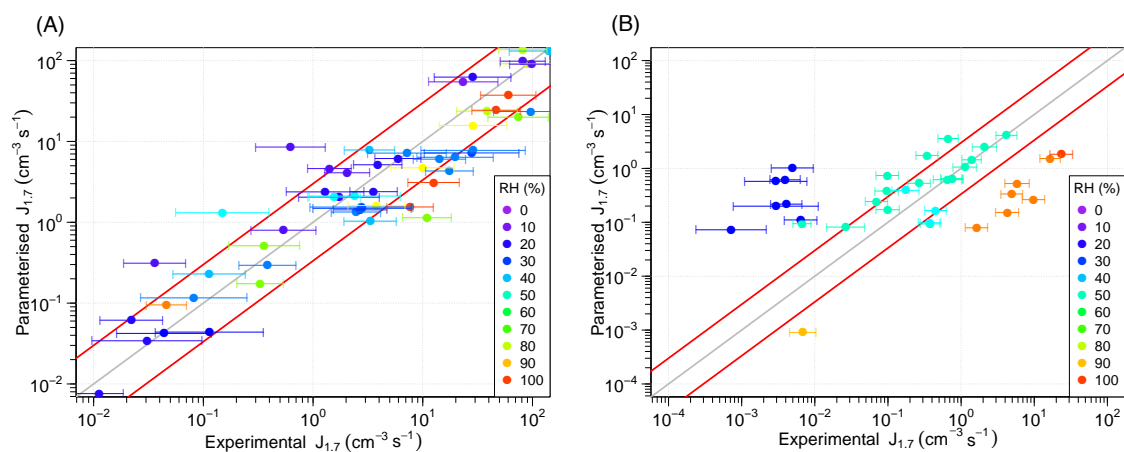
Figure S6: Dependence of the nucleation rate on relative humidity at (A) 208 and 223 K and (B) 298 K. The parameterization (y-axis) is independent of RH (color scale) while the experimental data (x-axis) have a relatively strong dependence at 298 K as described in the text. The 1:1 line is shown in grey and red lines indicate a factor three change in J.
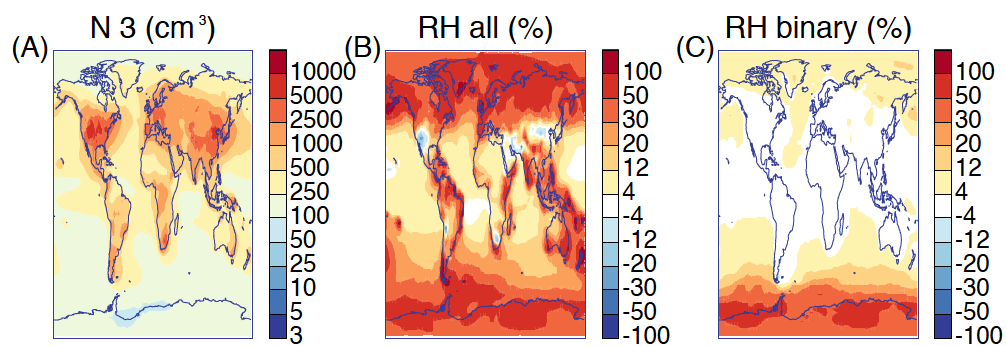
Figure S7: Annual mean modelled concentrations of 3 nm particles at cloud base level and changes to these concentrations when a test function approximately describing the dependence of the inorganic nucleation rate on RH is included, (B) for inorganic nucleation only and (C) for all nucleation.
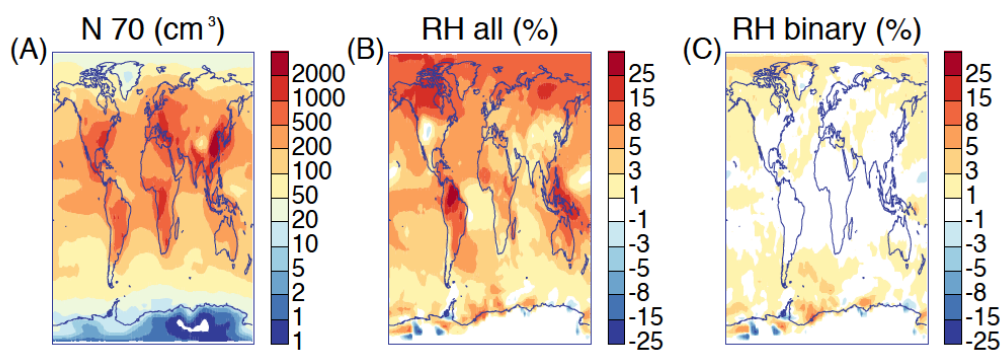
Figure S8: Annual mean modelled concentrations of soluble 70 nm particles at cloud base level and changes to these concentrations when a test function approximately describing the dependence of the inorganic nucleation rate on RH is included, (B) for inorganic nucleation only and (C) for all nucleation. To exclude numerical effects, changes are not plotted when concentrations are below $5\,\mathrm{cm}^{-3}$.
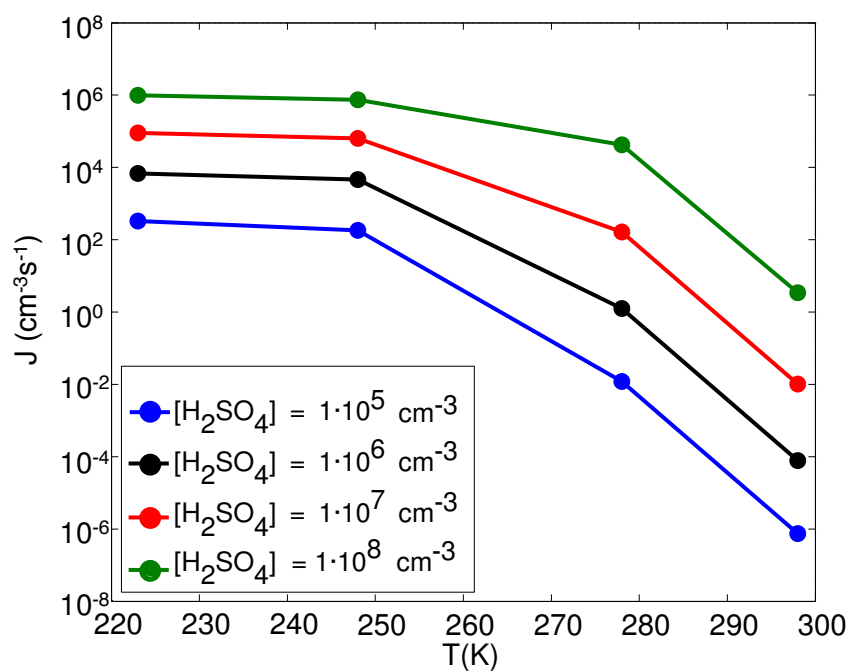
Figure S9: Proxy nucleation rates for organic nucleation of MBTCA with sulfuric acid calcu-lated from the ACDC model coupled to a quantum chemistry simulation of Gibbs free energies. The temperature dependence of the nucleation rate is shown for four different values of $[H_2SO_4]$ with 1 pptv of MBTCA.
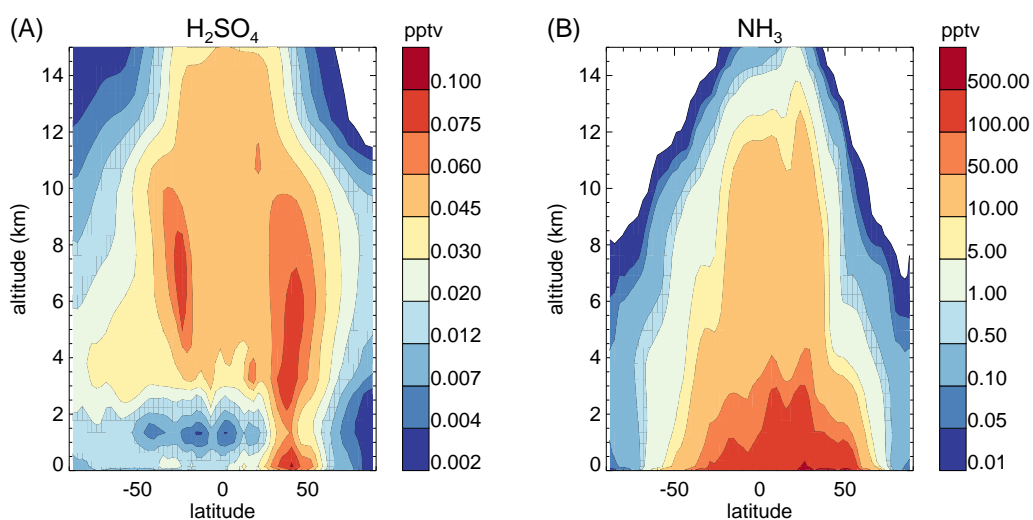
Figure S10: Vertical profiles of nucleating inorganic trace gases. Concentration of (A),$[H_2SO_4]$ modeled using GLOMAP-bin; (B), gas-phase $[NH_3]$ obtained from a GLOMAP-mode simulation using the EDGAR Emissions Inventory (*51*) and the particulate ammonium dissolution solver of Ref. (*94*). Both figures are annual mean values for 2008 and concentrations are shown as zonal means.
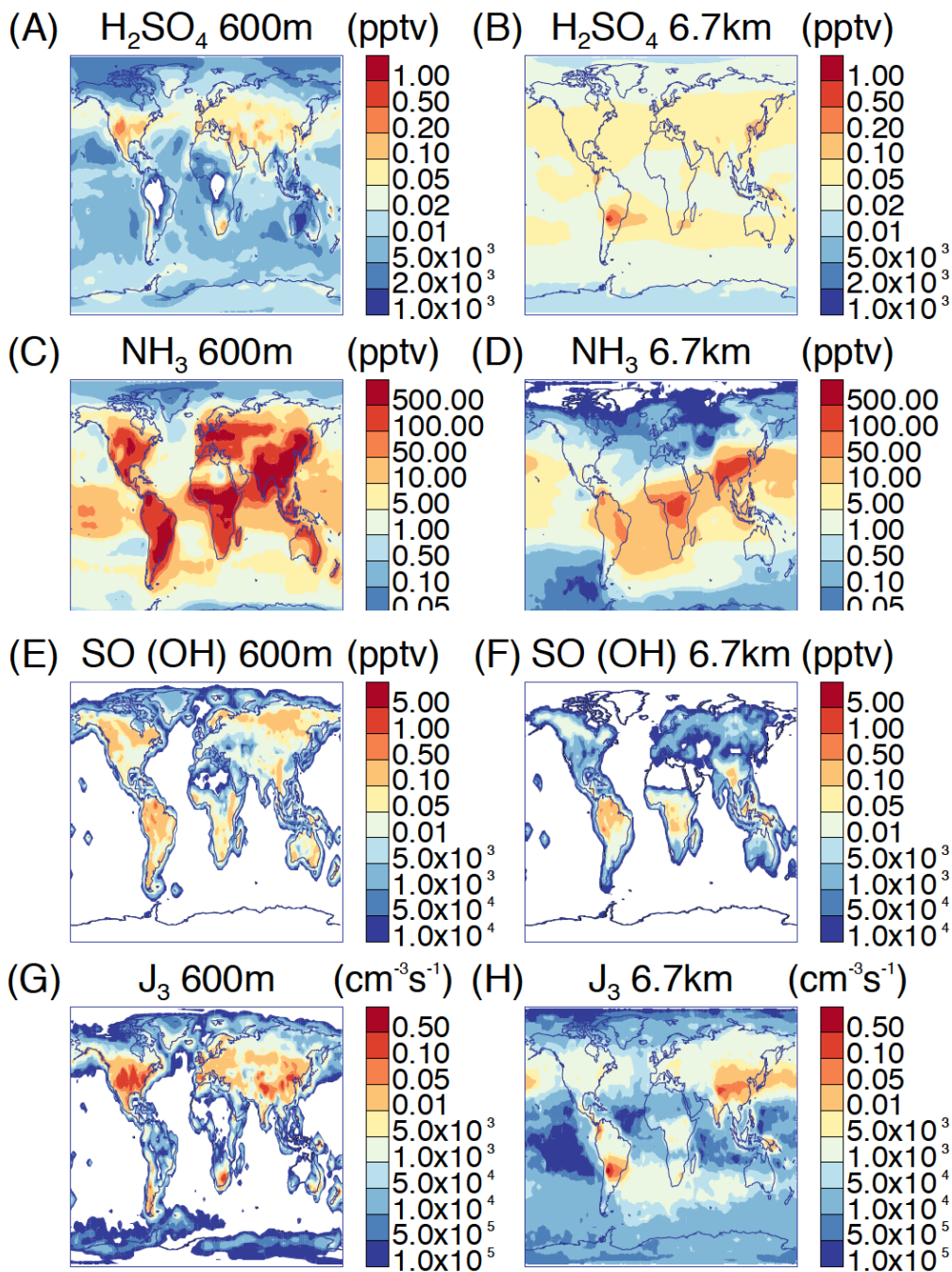
Figure S11: Horizontal maps of nucleating trace gases and resulting nucleation rates at 3 nm at mean altitudes of 600 m and 6.7 km. All figures are annual mean values for 2008. Concentrations of (A, B) $[H_2SO_4]$ (C, D), gas-phase $[NH_3]$, and (E, F) BioOxOrg (labelled as SO, 'secondary organic' for brevity) molecules participating in nucleation (the oxidation products of alpha-pinene with the hydroxyl radical, OH). As the BioOxOrg yield is not measured in Ref. (*24*), but is included in the nucleation rate constant, a yield of 100% is assumed in plots (E) and (F). Plots (G, H) show the formation rates of 3 nm particles. The annual average rate shown here is more indicative of the frequency of nucleation events than the nucleation rate during any given event.
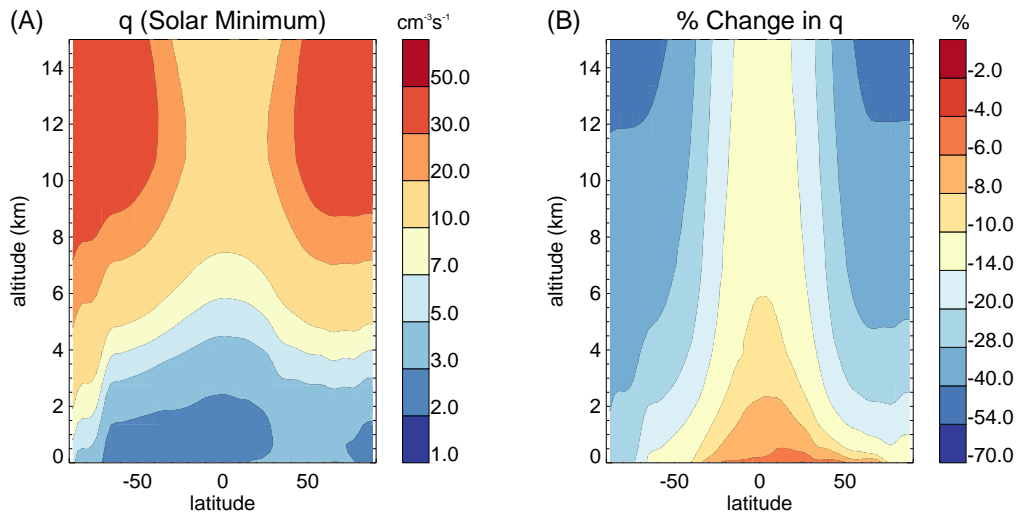
Figure S12: Annual mean ion-pair production rate q for the solar minimum of 2008 (A), and percentage change over the solar cycle (B). The rate is calculated from the look-up tables of Ref. (*101*). Ionization rates reach a maximum over the poles, where the Earth's magnetic field is weakest, and at altitudes of 10-15 km. At these altitudes, the high density of air compared to higher in the stratosphere increases the probability of interaction of a cosmic ray. At lower altitudes, essentially all of the primary GCRs have already interacted and only penetrating secondary particles survive. Radon is included from Ref. (*103*).
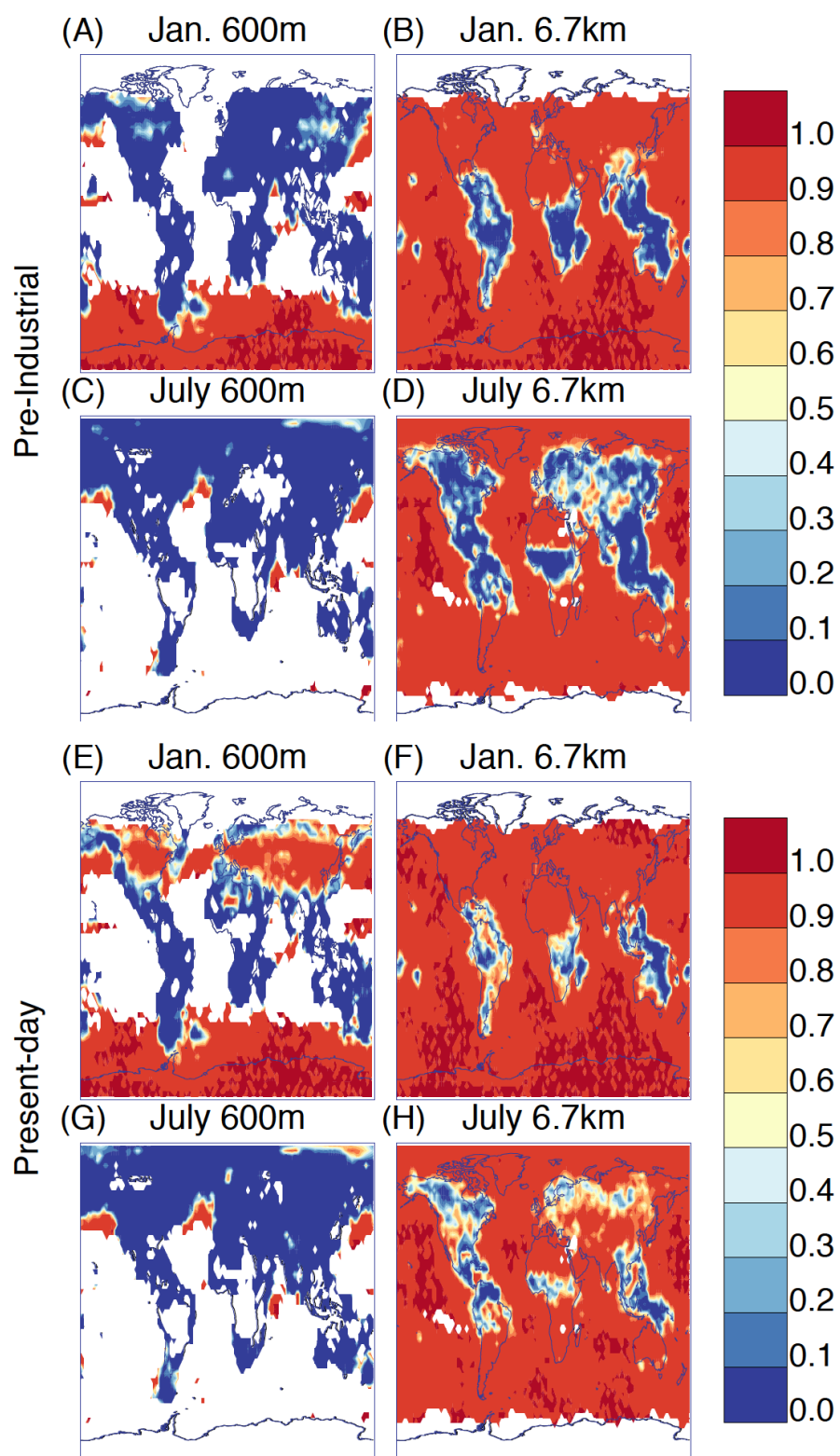
Figure S13: Fraction of total nucleation rate due to inorganic nucleation at two altitudes and for two months for pre-industrial and present-day conditions. The organic nucleation is assumed to be temperature-independent.
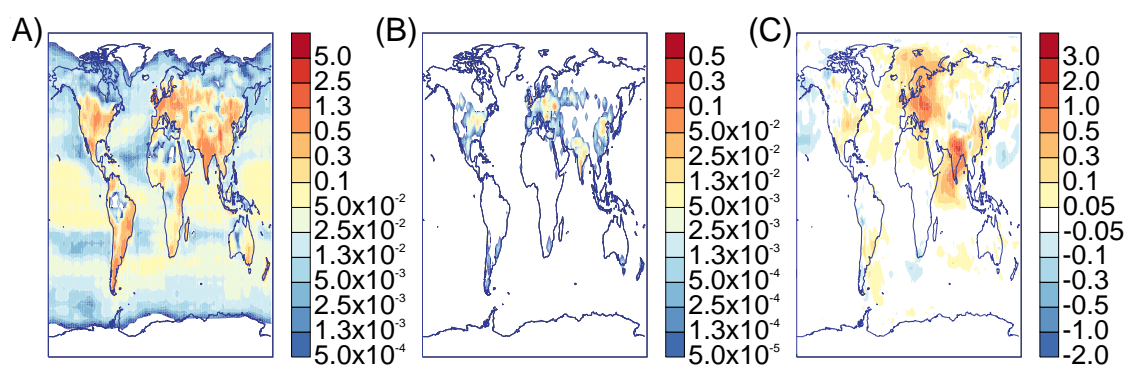
Figure S14: Results of preliminary investigation of amine-driven nucleation. Concentrations of amines in pptv (A), nucleation rates for the amine-driven mechanism in $\mathrm{cm^{-3}s^{-1}}$ (B), and changes to CCN concentrations (in %) when nucleation involving amines is included in our global model (C). All three subfigures are annual averages over grid boxes within approximately 500 m altitude of the surface.
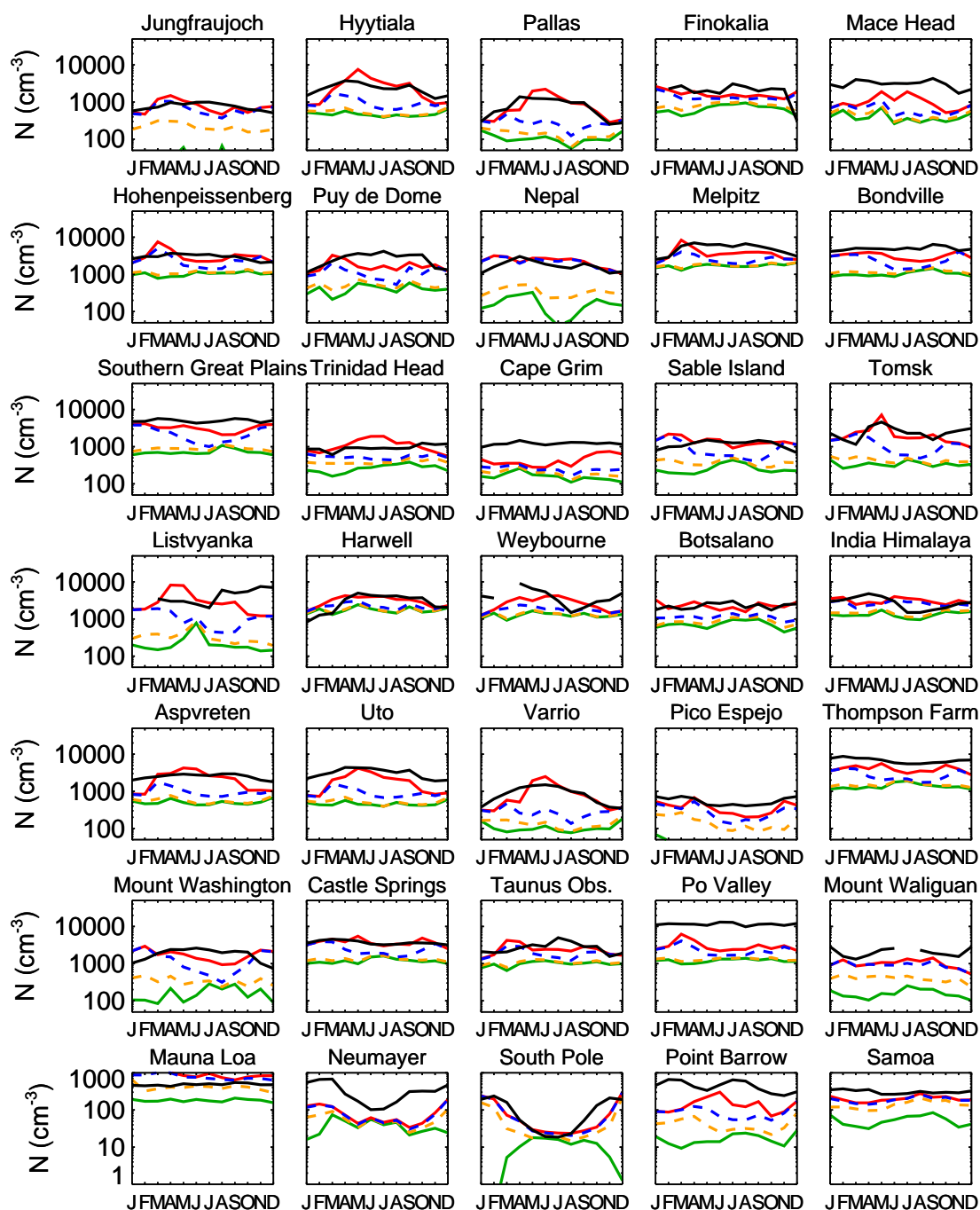
Figure S15: Comparison of modeled aerosol concentrations with measurements made at surface sites and mountain tops (*43*). Black line: measurements. Red line: current model. Blue line: neutral and ion-induced inorganic nucleation and primary particles only. Orange line: primary particles and binary neutral nucleation only. Green line: primary particles only.
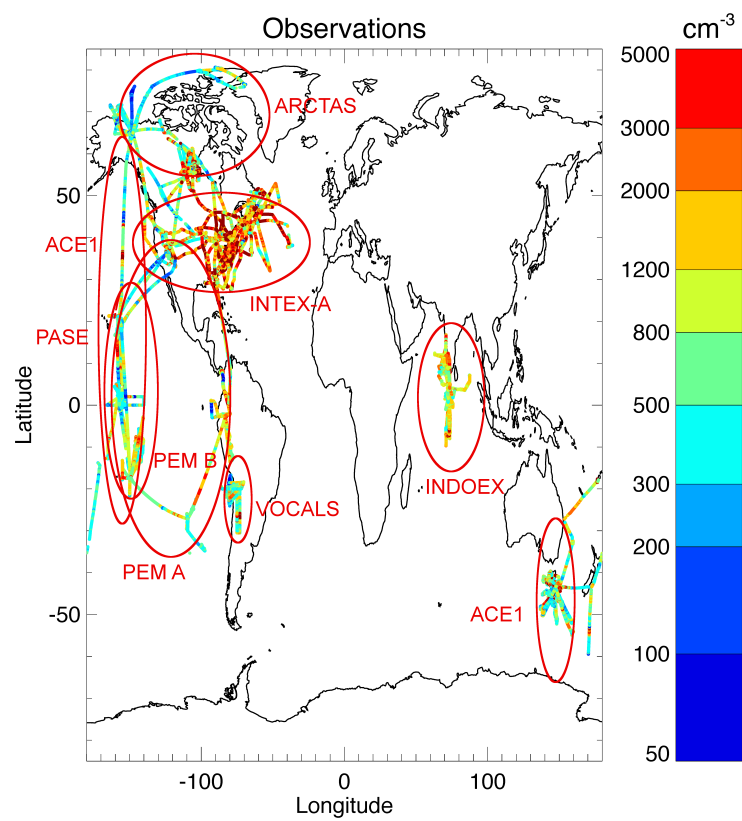
Figure S16: The locations of aircraft measurements used to compare the model with observations in Figure S17.
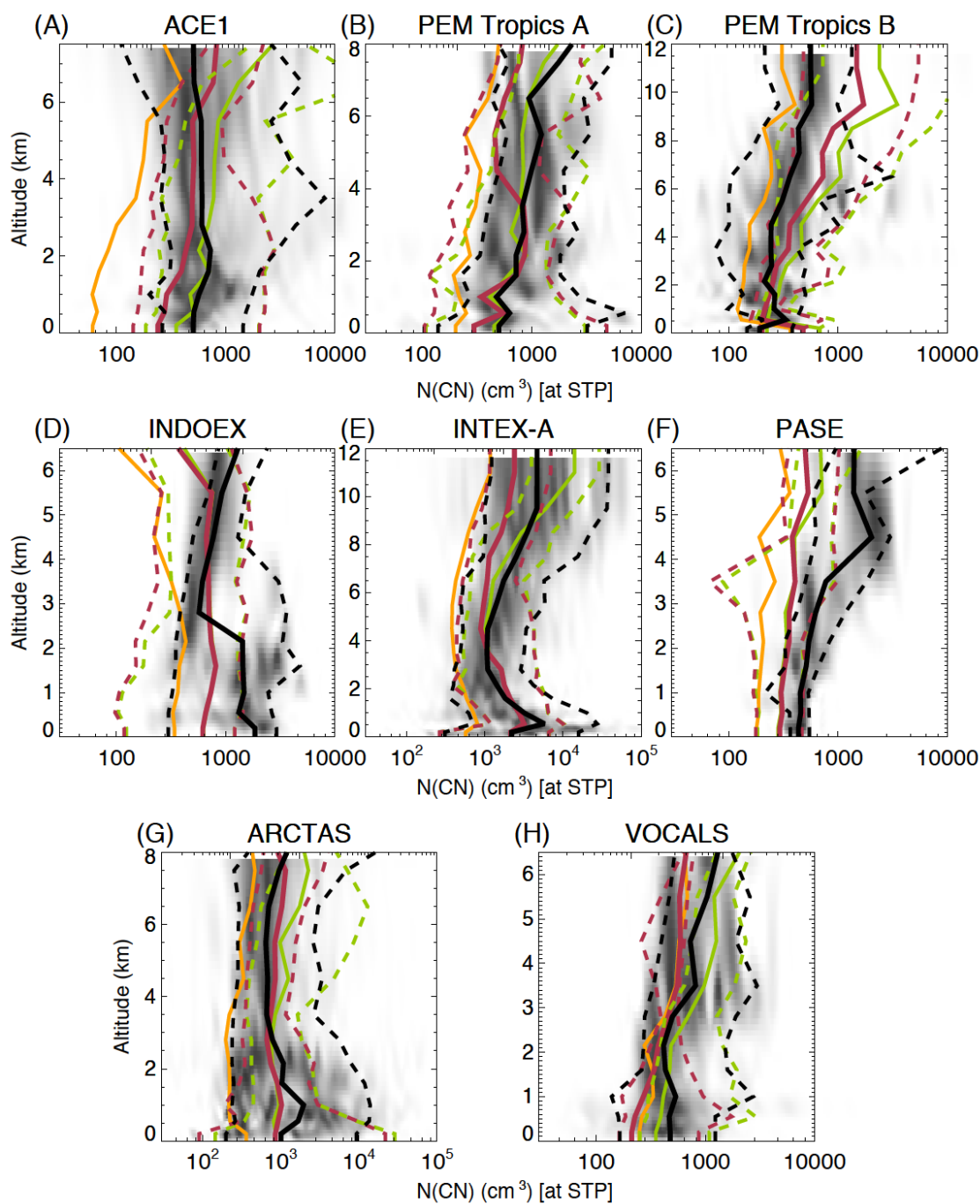
Figure S17: Comparison of modeled and observed vertical profiles of particle concentrations in the atmosphere. Solid lines indicate the median, with dashed lines showing the 10% and 90% deciles. Modeled distributions are shown by red lines when all processes are included, and by orange lines when only primary particles and binary neutral nucleation are included (deciles not shown in the latter case, for clarity). A previous version of the model with nucleation according to Refs. (106) and (24) is shown by the green lines. Atmospheric observations are shown by black lines. The greyscale background shows the distribution of atmospheric observations. The normalised mean differences between the modeled and observed distributions are summarised in Table S5.
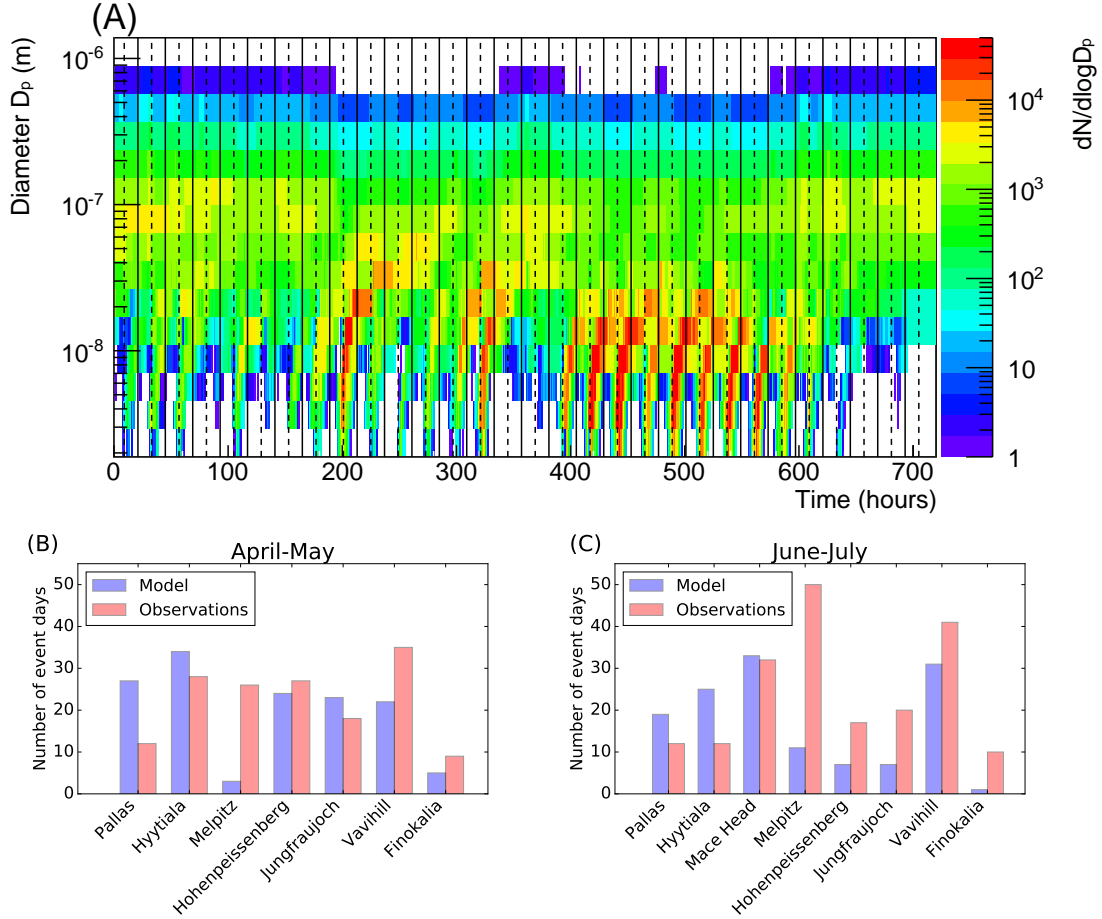
Figure S18: Modelled size distributions in April 2008 at Hyytiälä, Finland (A), and comparison of modeled and observed frequencies of nucleation events across April and May (B) and June and July (C). In subfigure (A), midnight local time is marked with solid lines and midday with dashed lines. Thirteen days (nucleation 'bananas' at approximately hours 200, 225, 302, 325, 398, 422, 446, 470, 494, 518, 542, 566, and 590) meet our criteria to be nucleation event days. While other pseudo-nucleation events are visible on this plot, they do not meet the criteria defined in Ref. (*129*) (see discussion in text). The observations in subfigures (B) and (C) were extracted from Ref. (*128*), Appendix A, which provides the fractions of event, non-event and undefined days out of all analyzed days in a given month. We multiply the fraction of event days by the length of each month and assume undefined days are non-events (or would not meet the criteria applied to the modeled events).
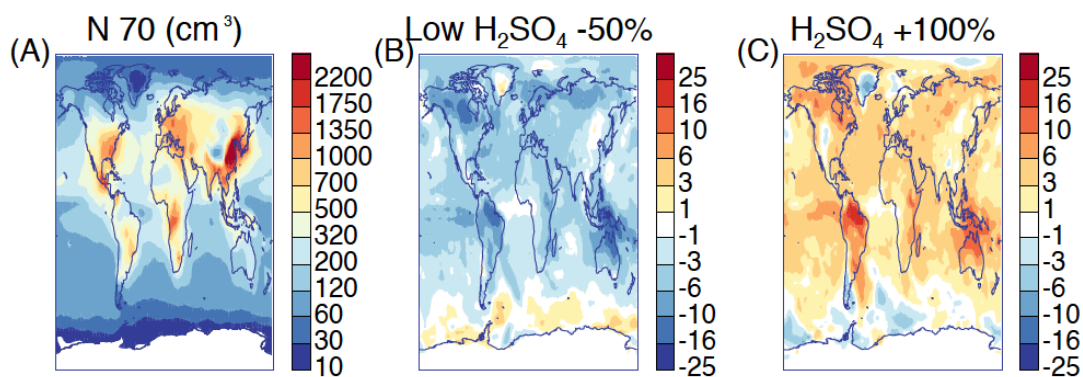
Figure S19: Effect of sulfuric acid uncertainties for organic nucleation. (A) Nominal soluble particle concentrations above a 70 nm threshold diameter (N70), averaged for March-June inclusive. (B) Change of N70 (%) when H_2SO_4 concentrations are reduced by 50%. (C) Change of N70 (%) when H_2SO_4 concentrations are increased by 100%. To exclude numerical effects, changes are not plotted when concentrations are below $5\,cm^{-3}$.
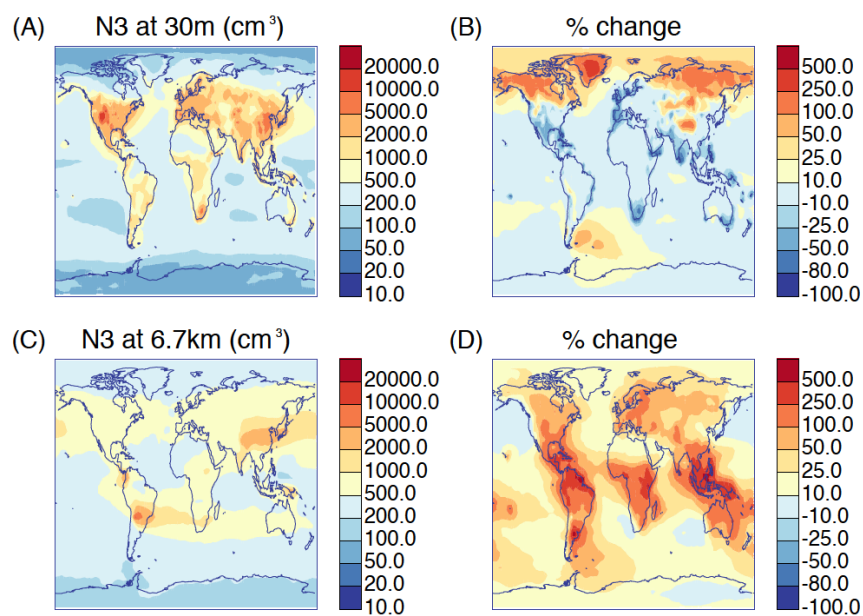
Figure S20: Sensitivity of soluble particle concentrations to the temperature dependence of the organic nucleation rate. (A),(C) Concentrations of soluble particles of at least 3 nm diameter at the surface and at 6.7 km altitude with temperature-independent organic nucleation rates. (B),(D) Percentage changes in those concentrations when a temperature dependence from a quantum chemistry simulation (Sect. 10) is introduced into the aerosol model.
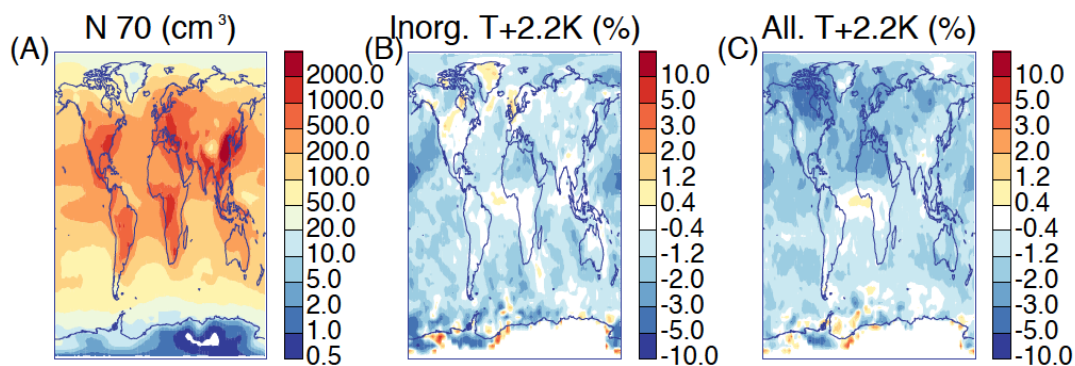
Figure S21: Total particle number concentrations above 70 nm diameter (N70) at cloud base level in the soluble distribution (A) and the perturbations to these concentrations resulting from a change to nucleation when the temperature is increased by 2.2 K under the assumptions that (B) the organic nucleation rates are independent of temperature and (C) that they depend on temperature according to quantum chemistry simulations described in Sect. 10. To exclude numerical effects, changes are not plotted when concentrations are below $5\,\mathrm{cm}^{-3}$.

Table S1: Parameters in the fit to inorganic nucleation rates (Sect. 8) as a function of sulfuric acid, ammonia, ion production rate and temperature. The fit is performed with sulfuric acid and ammonia concentrations in units of 10^6 cm^{-3}. The subscripts b and t refer to binary and ternary inorganic nucleation while n and i refer to neutral and ion-induced nucleation.

Parameter	Value	Parameter	Value
$p_{b,n}$	3.95	$p_{b,i}$	3.37
$u_{b,n}$	9.70	$u_{b,i}$	-11.5
$v_{b,n}$	12.6	$v_{b,i}$	25.5
$w_{b,n}$	-0.00707	$w_{b,i}$	0.181
$p_{t,n}$	2.89	$p_{t,i}$	3.14
$u_{t,n}$	182	$u_{t,i}$	-23.8
$v_{t,n}$	1.20	$v_{t,i}$	37.0
$w_{t,n}$	-4.19	$w_{t,i}$	0.227
$p_{A,n}$	8.00	$p_{A,i}$	3.07
a_n	1.6×10^{-6}	a_i	0.00485

Table S2: Parameters in the cross-checking fit to nucleation rates as a function of sulfuric acid, ammonia, ion production rate and temperature, with a simpler temperature dependence (Sect. 8). The fit is performed with sulfuric acid and ammonia concentrations in units of $10^6\,\mathrm{cm}^{-3}$. The subscripts b and t refer to binary and ternary inorganic nucleation while n and i refer to neutral and ion-induced nucleation.

Parameter	Value	Parameter	Value
$p_{b,n}$	3.62	$p_{b,i}$	2.73
$u_{b,n}$	46.3	$u_{b,i}$	24.1
$v_{b,n}$	245	$v_{b,i}$	166
$p_{t,n}$	2.82	$p_{t,i}$	2.86
$u_{t,n}$	41.2	$u_{t,i}$	18.3
$v_{t,n}$	252	$v_{t,i}$	208
$p_{A,n}$	6.76	$p_{A,i}$	5.0
a_n	1.3×10^{-4}	a_i	5.0×10^{-7}

Table S3: Emissions of primary aerosols and precursor gases for nucleation and growth processes. Sulfur gas species are in $TgSyr^{-1}$, carbonaceous species are $TgCyr^{-1}$, sea salt is $TgNaClyr^{-1}$, and ammonia is $TgNyr^{-1}$.

Emission	Budget $Tgyr^{-1}$	Diameter nm	Reference
Sea salt	1300	Parametrized	Martensson et al. (2003) (*86, 87*)
Black Carbon (fires)	3.0	150	van der Werf et al. (2003), Stier et al. (2005) (*132, 133*)
Black Carbon (fossil fuels)	3.0	60	Bond et al. (2004), Stier et al. (2005) (*133, 134*)
Black Carbon (bio-fuels)	1.6	150	Bond et al. (2004), Stier et al. (2005) (*133, 134*)
Organic carbon (fires)	24.8	150	van der Werf et al. (2003), Stier et al. (2005) (*132, 133*)
Organic carbon (fossil fuels)	2.4	80	Bond et al. (2004), Stier et al. (2005) (*133, 134*)
Organic carbon (bio-fuels)	6.5	150	Bond et al. (2004), Stier et al. (2005) (*133, 134*)
Primary sulfate	1.67	60,150,1500	Dentener et al. (2006) (*85*)
DMS	18.7	-	Kettle & Andreae (2000) (*81*)
Monoterpenes	127.0	-	Guenther et al. (1995) (*84*)
SO_2 (Anthropogenic)	54.3	-	Cofala et al. (2007), Dentener et al. (2006) (*83, 85*)
SO_2 (Volcanic)	12.6	-	Andres & Kasgnoc (1998) (*135*)
SO_2 (Biomass)	4.1	-	Dentener et al. (2006), van der Werf et al. (2003) (*85, 132*)
Ammonia	54	-	Bouwman et al. (1997) (*51*)

Table S4: Normalized mean model bias at surface sites listed in Fig. S15 (*43*), in percent. The 'cut-off' column refers to the cut-off of the condensation particle counter at the site. The 'Primary' column gives the model bias when nucleation is switched off altogether. The 'binary neut.' column gives the model bias when only primary particle emissions and binary neutral nucleation are included. The 'inorganic' column gives the model bias when primary particles, neutral and ion-induced binary and ternary inorganic nucleation (with ammonia) are included in the model. The 'overall' column gives the bias of the full model.

Site	Cut-off (nm)	Primary	Bin. neut.	Inorganic	Overall
Jungfraujoch	10	-96	-71	-16	2
Hyytiala	3	-79	-77	-59	12
Pallas	10	-86	-82	-64	9
Finokalia	10	-65	-57	-26	-12
Mace Head	10	-86	-84	-78	-66
Hohenpeissenberg	3	-65	-61	-18	8
Puy de Dome	10	-84	-80	-56	-34
Nepal	3	-90	-80	23	28
Melpitz	3	-66	-64	-48	-25
Bondville	14	-79	-76	-49	-36
Southern Great Plains	10	-85	-82	-53	-34
Trinidad Head	14	-72	-59	-43	17
Cape Grim	3	-86	-83	-79	-63
Sable Island	10	-77	-67	-18	23
Tomsk	3	-86	-82	-54	-12
Listvyanka	3	-93	-89	-65	-5
Harwell	10	-42	-39	-26	2
Weybourne	10	-57	-55	-41	-11
Botsalano	10	-68	-62	-50	1
India Himalaya	10	-53	-47	-8	9
Aspvreten	3	-79	-77	-60	-12
Uto	7	-85	-83	-70	-39
Varrio	8	-87	-84	-67	0
Pico Espejo	10	-95	-72	-46	-31
Thompson Farm	7	-79	-77	-59	-41
Mount Washington	10	-91	-81	-25	-2
Castle Springs	7	-67	-64	-31	1
Taunus Obs.	10	-64	-61	-32	-11
Po Valley	3	-89	-88	-79	-73
Mount Waliguan	13	-91	-79	-51	-46
Mauna Loa	14	-62	-15	60	82
Neumayer	14	-89	-83	-76	-75
South Pole	14	-91	-46	-18	-16
Point Barrow	14	-96	-90	-80	-68
Samoa	14	-82	-55	-39	-35
Zugspitze	12	-86	-76	-21	3
All		-78	-74	-50	-25
All June-Aug		-78	-75	-64	-29
All Dec-Feb		-75	-69	-35	-29

Table S5: Normalized mean bias (NMB) in particle concentrations at 3 nm diameter of model simulations relative to aircraft observations. Only including binary neutral nucleation calculated according to the CLOUD experimental parameterization (first column) leads to a strong under-prediction of particle number concentrations (see Figure 3). Previous versions of GLOMAP, including organic nucleation (*24*) and sulfuric acid binary nucleation according to Ref. (*106*), over-predict particle concentrations by 16% on average (second column). In the current model (last column), on average, particle concentrations are under-predicted by 39%. This suggests nucleation or growth rates at high altitude may be underestimated, possibly due to our neglecting the temperature dependence of organic nucleation rates.

Campaign	Binary only (%)	Organic (%)	This model (%)
ACE1	-82	30	-31
PEM Tropics A	-67	-16	-30
PEM Tropics B	-55	82	5.8
INDOEX	-66	-32	-44
INTEX-A	-86	-16	-58
PASE	-66	-42	-42
ARCTAS	-82	39	-19
VOCALS	-50	2.9	-46
All campaign data	-78	16	-39

Table S6: Summary of changes to soluble 70 nm particle concentrations (N70) in the model as a result of perturbations to model inputs specified. Changes are either averages over simulations of an entire year or of the March-June period, as specified in the 'Period' column. Part a) details uncertainties related to the parameterization of CLOUD formation rates, part b) uncertainties in the aerosol model inputs. Only two of these are presented here as dedicated studies are documented elsewhere (47). In some cases (e.g. relative humidity, RH) only a single perturbation was performed to estimate the uncertainty: in these cases only one number features in the last colum.

	Model parameter	Variation	Period	Change to N70 (%)
a)	CLOUD measurements and parameterization			
	Nucleation rate	$\pm$Factor 2.5	Mar-Jun	$+2.0/-2.1$
	RH dependence of J (Sect. 9)	Parameterize	Annual	$+6.0$
	RH dep. of binary J (Sect. 9)	Parameterize	Annual	$+0.7$
	Effect of T on org. J (Sect. 20)	Introduce from MBTCA	Annual	-0.4
	Inorg. J parameterization	Remove binary neutral	Mar-Jun	-0.1
	Organic J param.	Use EUCAARI	Annual	$+2.6$
	H_2SO_4	$+100\%/-50\%$ (in inorg. J)	Mar-Jun	$+3.2/-2.9$
	H_2SO_4	$+100\%/-50\%$ (in org. J)	Mar-Jun	$+4.1/-3.7$
	H_2SO_4	Temperature effects: factor 2	Mar-Jun	-0.2
	NH_3	CLOUD lower/upper limits	Mar-Jun	$-0.8/+0.4$
b)	GLOMAP model uncertainties			
	Terpene emissions	$+100\%/-50\%$	Mar-Jun	$+8.9/-6.9$
	$1.7-3$ nm growth rates	$+50\%/-50\%$	Mar-Jun	$+0.5/-0.5$

Table S7: Summary of fractions of nucleation via the five pathways that we can resolve most accurately (binary neutral, binary ion-induced, ternary inorganic neutral, ternary inorganic ion-induced and ternary organic) in different sensitivity tests. The 'realistic T-depend' row refers to the results when the organic nucleation rates are multiplied by $\exp(-(T - 278)/10)$, which we consider to represent the most likely temperature dependence for the organic nucleation rate. The 'RH. dep. bin.' row refers to the results when the smooth function parametrising the RH dependence of the nucleation rate (Sect. 9) is applied to binary nucleation only. The first five rows above the horizontal line are based on annually averaged results, the second are estimates derived from runs performed for March-June only (to save CPU) and scaled to represent the annual average. All results are for averages over the troposphere within 15 km of the surface.

	Bin. neut.	Bin. IIN	Tern. neut.	Tern. IIN	Organic
Baseline run	0.026	0.116	0.538	0.113	0.207
Baseline January	0.056	0.087	0.551	0.159	0.147
Baseline July	0.022	0.103	0.567	0.074	0.234
MBTCA T-depend.	0.010	0.044	0.219	0.042	0.686
Realistic T-depend.	0.017	0.080	0.386	0.083	0.433
RH depend.	0.019	0.087	0.435	0.090	0.369
RH. dep. bin.	0.033	0.163	0.505	0.105	0.193
EUCAARI organic nuc.	0.028	0.126	0.557	0.126	0.163
Baseline Mar-Jun	0.018	0.097	0.529	0.096	0.260
16-parameter version	0.012	0.146	0.279	0.375	0.189
Low H2SO4 inorg.	0.0044	0.038	0.329	0.056	0.573
High H2SO4 inorg.	0.0491	0.192	0.538	0.118	0.102
Low H2SO4 org.	0.0204	0.116	0.606	0.123	0.135
High H2SO4 inorg.	0.0131	0.072	0.397	0.068	0.450
Low NH3 param.	0.0202	0.092	0.533	0.118	0.236
High NH3 param.	0.0286	0.058	0.489	0.113	0.311
No binary neutral	0.0000	0.090	0.455	0.161	0.293
High terpene emissions	0.0161	0.092	0.491	0.088	0.314
Low terpene emissions	0.0184	0.103	0.551	0.109	0.220
High $1 - 3\,\text{nm}$ growth rates	0.0171	0.095	0.511	0.096	0.280
Low $1 - 3\,\text{nm}$ growth rates	0.0175	0.098	0.524	0.099	0.262

Additional Data Table S1 (separate file): A table in comma-separated-value format containing the nucleation rates we use in our parameterization of inorganic nucleation is provided. It contains nucleation rate (in $\mathrm{cm}^{-3}\mathrm{s}^{-1}$), and the corresponding values of temperature, in Kelvin, sulfuric acid concentration in units of $10^6\,\mathrm{cm}^{-3}$, ammonia concentration in parts per trillion, ionization rate ($\mathrm{cm}^{-3}\mathrm{s}^{-1}$), and relative humidity (in %).

References and Notes

1. M. Kulmala, L. Laakso, K. E. J. Lehtinen, I. Riipinen, M. Dal Maso, T. Anttila, V. M. Kerminen, U. Hõrrak, M. Vana, H. Tammet, Initial steps of aerosol growth. *Atmos. Chem. Phys.* **4**, 2553–2560 (2004). [doi:10.5194/acp-4-2553-2004](doi:10.5194/acp-4-2553-2004)

2. C. A. Brock, P. Hamill, J. C. Wilson, H. H. Jonsson, K. R. Chan, Particle formation in the upper tropical troposphere: A source of nuclei for the stratospheric aerosol. *Science* **270**, 1650–1653 (1995). doi:10.1126/science.270.5242.1650

3. A. D. Clarke, Atmospheric nuclei in the remote free-troposphere. *J. Atmos. Chem.* **14**, 479–488 (1992). [doi:10.1007/BF00115252](doi:10.1007/BF00115252)

4. J. Merikanto, D. V. Spracklen, G. W. Mann, S. J. Pickering, K. S. Carslaw, Impact of nucleation on global CCN. *Atmos. Chem. Phys.* **9**, 8601–8616 (2009). [doi:10.5194/acp-9-8601-2009](doi:10.5194/acp-9-8601-2009)

5. M. Wang, J. E. Penner, Aerosol indirect forcing in a global model with particle nucleation. *Atmos. Chem. Phys.* **9**, 239–260 (2009). [doi:10.5194/acp-9-239-2009](doi:10.5194/acp-9-239-2009)

6. F. Yu, G. Luo, Simulation of particle size distribution with a global aerosol model: Contribution of nucleation to aerosol and CCN number concentrations. *Atmos. Chem. Phys.* **9**, 7691–7710 (2009). [doi:10.5194/acp-9-7691-2009](doi:10.5194/acp-9-7691-2009)

7. J. Kirkby, J. Curtius, J. Almeida, E. Dunne, J. Duplissy, S. Ehrhart, A. Franchin, S. Gagné, L. Ickes, A. Kürten, A. Kupc, A. Metzger, F. Riccobono, L. Rondo, S. Schobesberger, G. Tsagkogeorgas, D. Wimmer, A. Amorim, F. Bianchi, M. Breitenlechner, A. David, J. Dommen, A. Downard, M. Ehn, R. C. Flagan, S. Haider, A. Hansel, D. Hauser, W. Jud, H. Junninen, F. Kreissl, A. Kvashin, A. Laaksonen, K. Lehtipalo, J. Lima, E. R. Lovejoy, V. Makhmutov, S. Mathot, J. Mikkilä, P. Minginette, S. Mogo, T. Nieminen, A. Onnela, P. Pereira, T. Petäjä, R. Schnitzhofer, J. H. Seinfeld, M. Sipilä, Y. Stozhkov, F. Stratmann, A. Tomé, J. Vanhanen, Y. Viisanen, A. Vrtala, P. E. Wagner, H. Walther, E. Weingartner, H. Wex, P. M. Winkler, K. S. Carslaw, D. R. Worsnop, U. Baltensperger, M. Kulmala, Role of sulphuric acid, ammonia and galactic cosmic rays in atmospheric aerosol nucleation. *Nature* **476**, 429–433 (2011). Medline doi:10.1038/nature10343

8. R. Zhang, I. Suh, J. Zhao, D. Zhang, E. C. Fortner, X. Tie, L. T. Molina, M. J. Molina, Atmospheric new particle formation enhanced by organic acids. *Science* **304**, 1487–1490 (2004). Medline doi:10.1126/science.1095139

9. S. M. Ball, D. R. Hanson, F. L. Eisele, P. H. McMurry, Laboratory studies of particle nucleation: Initial results for H_2SO_4, H_2O, and NH_3 vapors. *J. Geophys. Res., D, Atmospheres* **104**, 23709–23718 (1999). [doi:10.1029/1999JD900411](doi:10.1029/1999JD900411)

10. D. R. Benson, J. H. Yu, A. Markovich, S.-H. Lee, Ternary homogeneous nucleation of H_2SO_4, NH_3, and H_2O under conditions relevant to the lower troposphere. *Atmos. Chem. Phys.* **11**, 4755–4766 (2011). [doi:10.5194/acp-11-4755-2011](doi:10.5194/acp-11-4755-2011)

11. R. Makkonen, A. Asmi, H. Korhonen, H. Kokkola, S. Ja¨rvenoja, P. Ra¨isa¨nen, K. E. J. Lehtinen, A. Laaksonen, V.-M. Kerminen, H. Ja¨rvinen, U. Lohmann, R. Bennartz, J. Feichter, M. Kulmala, Sensitivity of aerosol concentrations and cloud properties to

nucleation and secondary organic distribution in ECHAM5-HAM global circulation model. *Atmos. Chem. Phys.* **9**, 1747–1766 (2009). doi:10.5194/acp-9-1747-2009

12. P. J. Adams, J. H. Seinfeld, Predicting global aerosol size distributions in general circulation models. *J. Geophys. Res. Atmos.* **107**, AAC 4-1–AAC 4-23 (2002). doi:10.1029/2001JD001010

13. D. V. Spracklen, K. J. Pringle, K. S. Carslaw, M. P. Chipperfield, G. W. Mann, A global off-line model of size-resolved aerosol microphysics: I. Model development and prediction of aerosol properties. *Atmos. Chem. Phys.* **5**, 2227–2252 (2005). doi:10.5194/acp-5-2227-2005

14. S.-H. Lee, J. M. Reeves, J. C. Wilson, D. E. Hunton, A. A. Viggiano, T. M. Miller, J. O. Ballenthin, L. R. Lait, Particle formation by ion nucleation in the upper troposphere and lower stratosphere. *Science* **301**, 1886–1889 (2003). Medline doi:10.1126/science.1087236

15. J. Kazil, P. Stier, K. Zhang, J. Quaas, S. Kinne, D. O'Donnell, S. Rast, M. Esch, S. Ferrachat, U. Lohmann, J. Feichter, Aerosol nucleation and its role for clouds and Earth's radiative forcing in the aerosol-climate model ECHAM5-HAM. *Atmos. Chem. Phys.* **10**, 10733–10752 (2010). doi:10.5194/acp-10-10733-2010

16. M. Kulmala, H. Vehkamäki, T. Petäjä, M. Dal Maso, A. Lauri, V.-M. Kerminen, W. Birmili, P. H. McMurry, Formation and growth rates of ultrafine atmospheric particles: A review of observations. *J. Aerosol Sci.* **35**, 143–176 (2004). doi:10.1016/j.jaerosci.2003.10.003

17. H. Svensmark, E. Friis-Christensen, Variation of cosmic ray flux and global cloud coverage-a missing link in solar-climate relationships. *J. Atmos. Sol. Terr. Phys.* **59**, 1225–1232 (1997). doi:10.1016/S1364-6826(97)00001-1

18. G. Bond, B. Kromer, J. Beer, R. Muscheler, M. N. Evans, W. Showers, S. Hoffmann, R. Lotti-Bond, I. Hajdas, G. Bonani, Persistent solar influence on North Atlantic climate during the Holocene. *Science* **294**, 2130–2136 (2001). Medline doi:10.1126/science.1065680

19. U. Neff, S. J. Burns, A. Mangini, M. Mudelsee, D. Fleitmann, A. Matter, Strong coherence between solar variability and the monsoon in Oman between 9 and 6 kyr ago. *Nature* **411**, 290–293 (2001). Medline doi:10.1038/35077048

20. K. S. Carslaw, R. G. Harrison, J. Kirkby, Cosmic rays, clouds, and climate. *Science* **298**, 1732–1737 (2002). Medline doi:10.1126/science.1076964

21. J. Kirkby, Cosmic rays and climate. *Surv. Geophys.* **28**, 333–375 (2007). doi:10.1007/s10712-008-9030-6

22. M. Chen, M. Titcombe, J. Jiang, C. Jen, C. Kuang, M. L. Fischer, F. L. Eisele, J. I. Siepmann, D. R. Hanson, J. Zhao, P. H. McMurry, Acid-base chemical reaction model for nucleation rates in the polluted atmospheric boundary layer. *Proc. Natl. Acad. Sci. U.S.A.* **109**, 18713–18718 (2012). Medline doi:10.1073/pnas.1210285109

23. J. Almeida, S. Schobesberger, A. Kürten, I. K. Ortega, O. Kupiainen-Määttä, A. P. Praplan, A. Adamov, A. Amorim, F. Bianchi, M. Breitenlechner, A. David, J. Dommen, N. M. Donahue, A. Downard, E. Dunne, J. Duplissy, S. Ehrhart, R. C. Flagan, A. Franchin, R.

Guida, J. Hakala, A. Hansel, M. Heinritzi, H. Henschel, T. Jokinen, H. Junninen, M. Kajos, J. Kangasluoma, H. Keskinen, A. Kupc, T. Kurtén, A. N. Kvashin, A. Laaksonen, K. Lehtipalo, M. Leiminger, J. Leppä, V. Loukonen, V. Makhmutov, S. Mathot, M. J. McGrath, T. Nieminen, T. Olenius, A. Onnela, T. Petäjä, F. Riccobono, I. Riipinen, M. Rissanen, L. Rondo, T. Ruuskanen, F. D. Santos, N. Sarnela, S. Schallhart, R. Schnitzhofer, J. H. Seinfeld, M. Simon, M. Sipilä, Y. Stozhkov, F. Stratmann, A. Tomé, J. Tröstl, G. Tsagkogeorgas, P. Vaattovaara, Y. Viisanen, A. Virtanen, A. Vrtala, P. E. Wagner, E. Weingartner, H. Wex, C. Williamson, D. Wimmer, P. Ye, T. Yli-Juuti, K. S. Carslaw, M. Kulmala, J. Curtius, U. Baltensperger, D. R. Worsnop, H. Vehkamäki, J. Kirkby, Molecular understanding of sulphuric acid-amine particle nucleation in the atmosphere. *Nature* **502**, 359–363 (2013) Letter. Medline doi:10.1038/nature12663

24. F. Riccobono, S. Schobesberger, C. E. Scott, J. Dommen, I. K. Ortega, L. Rondo, J. Almeida, A. Amorim, F. Bianchi, M. Breitenlechner, A. David, A. Downard, E. M. Dunne, J. Duplissy, S. Ehrhart, R. C. Flagan, A. Franchin, A. Hansel, H. Junninen, M. Kajos, H. Keskinen, A. Kupc, A. Kürten, A. N. Kvashin, A. Laaksonen, K. Lehtipalo, V. Makhmutov, S. Mathot, T. Nieminen, A. Onnela, T. Petäjä, A. P. Praplan, F. D. Santos, S. Schallhart, J. H. Seinfeld, M. Sipilä, D. V. Spracklen, Y. Stozhkov, F. Stratmann, A. Tomé, G. Tsagkogeorgas, P. Vaattovaara, Y. Viisanen, A. Vrtala, P. E. Wagner, E. Weingartner, H. Wex, D. Wimmer, K. S. Carslaw, J. Curtius, N. M. Donahue, J. Kirkby, M. Kulmala, D. R. Worsnop, U. Baltensperger, Oxidation products of biogenic emissions contribute to nucleation of atmospheric particles. *Science* **344**, 717–721 (2014). Medline doi:10.1126/science.1243527

25. H. Vehkamäki, M. Kulmala, I. Napari, K. E. J. Lehtinen, C. Timmreck, M. Noppel, A. Laaksonen, An improved parameterization for sulfuric acid-water nucleation rates for tropospheric and stratospheric conditions. *J. Geophys. Res. Atmos.* **107**, AAC 3-1–AAC 3-10 (2002). doi:10.1029/2002JD002184

26. I. Napari, M. Noppel, H. Vehkamäki, M. Kulmala, Parametrization of ternary nucleation rates for H_2SO_4-NH_3-H_2O vapors. *J. Geophys. Res.* **107**, AAC 6-1–AAC 6-6 (2002). doi:10.1029/2002JD002132

27. S. D. D'Andrea, S. A. K. Ha¨kkinen, D. M. Westervelt, C. Kuang, E. J. T. Levin, V. P. Kanawade, W. R. Leaitch, D. V. Spracklen, I. Riipinen, J. R. Pierce, Understanding global secondary organic aerosol amount and size-resolved condensational behavior. *Atmos. Chem. Phys.* **13**, 11519–11534 (2013). doi:10.5194/acp-13-11519-2013

28. J. Jung, C. Fountoukis, P. J. Adams, S. N. Pandis, Simulation of in situ ultrafine particle formation in the eastern United States using PMCAMx-UF. *J. Geophys. Res. Atmos.* **115**, D03203 (2010). doi:10.1029/2009JD012313

29. L. K. Peters, A. A. Jouvanis, Numerical simulation of the transport and chemistry of CH_4 and CO in the troposphere. *Atmos. Environ.* **13**, 1443–1462 (1979). doi:10.1016/0004-6981(79)90113-6

30. H. Rodhe, I. Isaksen, Global distribution of sulfur compounds in the troposphere estimated in a height/latitude transport model. *J. Geophys. Res. Oceans* **85**, 7401–7409 (1980). doi:10.1029/JC085iC12p07401

31. J. Duplissy, J. Merikanto, A. Franchin, G. Tsagkogeorgas, J. Kangasluoma, D. Wimmer, H. Vuollekoski, S. Schobesberger, K. Lehtipalo, R. C. Flagan, D. Brus, N. M. Donahue, H. Vehkamäki, J. Almeida, A. Amorim, P. Barmet, F. Bianchi, M. Breitenlechner, E. M. Dunne, R. Guida, H. Henschel, H. Junninen, J. Kirkby, A. Kürten, A. Kupc, A. Määttänen, V. Makhmutov, S. Mathot, T. Nieminen, A. Onnela, A. P. Praplan, F. Riccobono, L. Rondo, G. Steiner, A. Tome, H. Walther, U. Baltensperger, K. S. Carslaw, J. Dommen, A. Hansel, T. Petäjä, M. Sipilä, F. Stratmann, A. Vrtala, P. E. Wagner, D. R. Worsnop, J. Curtius, M. Kulmala, Effect of ions on sulfuric acid-water binary particle formation: 2. Experimental data and comparison with QC-normalized classical nucleation theory. *J. Geophys. Res. Atmos.* **121**, 1752–1775 (2016). doi:10.1002/2015JD023539

32. A. Kürten, F. Bianchi, J. Almeida, O. Kupiainen-Määttä, E. M. Dunne, J. Duplissy, C. Williamson, J. Hakala, A. Hansel, M. Heinritzi, L. Ickes, T. Jokinen, J. Kangasluoma, J. Kim, J. Kirkby, A. Kupc, K. Lehipalo, M. Leiminger, V. Makhmutov, A. Onnela, I. Ortega, T. Petäjä, A. Praplan, F. Riccobono, M. P. Rissanen, L. Rondo, R. Schnitzhofer, A. Tomé, J. Tröstl, G. Tsagkogeorgas, P. Wagner, D. Wimmer, P. Ye, U. Baltensperger, K. Carslaw, M. Kulmala, J. Curtius, Experimental particle formation rates spanning tropospheric sulfuric acid and ammonia abundances, ion production rates, and temperatures. *J. Geophys. Res. Atmos.* 10.1002/2015JD023908 (2016).

33. A. Franchin, S. Ehrhart, J. Leppä, T. Nieminen, S. Gagné, S. Schobesberger, D. Wimmer, J. Duplissy, F. Riccobono, E. M. Dunne, L. Rondo, A. Downard, F. Bianchi, A. Kupc, G. Tsagkogeorgas, K. Lehtipalo, H. E. Manninen, J. Almeida, A. Amorim, P. E. Wagner, A. Hansel, J. Kirkby, A. Kürten, N. M. Donahue, V. Makhmutov, S. Mathot, A. Metzger, T. Petäjä, R. Schnitzhofer, M. Sipilä, Y. Stozhkov, A. Tomé, V.-M. Kerminen, K. Carslaw, J. Curtius, U. Baltensperger, M. Kulmala, Experimental investigation of ion–ion recombination under atmospheric conditions. *Atmos. Chem. Phys.* **15**, 7203–7216 (2015). doi:10.5194/acp-15-7203-2015

34. S. Schobesberger, A. Franchin, F. Bianchi, L. Rondo, J. Duplissy, A. Ku¨rten, I. K. Ortega, A. Metzger, R. Schnitzhofer, J. Almeida, A. Amorim, J. Dommen, E. M. Dunne, M. Ehn, S. Gagné, L. Ickes, H. Junninen, A. Hansel, V.-M. Kerminen, J. Kirkby, A. Kupc, A. Laaksonen, K. Lehtipalo, S. Mathot, A. Onnela, T. Petäjä, F. Riccobono, F. D. Santos, M. Sipilä, A. Tomé, G. Tsagkogeorgas, Y. Viisanen, P. E. Wagner, D. Wimmer, J. Curtius, N. M. Donahue, U. Baltensperger, M. Kulmala, D. R. Worsnop, On the composition of ammonia–sulfuric–acid–ion clusters during aerosol particle formation. *Atmos. Chem. Phys.* **15**, 55–78 (2015). doi:10.5194/acp-15-55-2015

35. S. Schobesberger, H. Junninen, F. Bianchi, G. Lönn, M. Ehn, K. Lehtipalo, J. Dommen, S. Ehrhart, I. K. Ortega, A. Franchin, T. Nieminen, F. Riccobono, M. Hutterli, J. Duplissy, J. Almeida, A. Amorim, M. Breitenlechner, A. J. Downard, E. M. Dunne, R. C. Flagan, M. Kajos, H. Keskinen, J. Kirkby, A. Kupc, A. Kürten, T. Kurtén, A. Laaksonen, S. Mathot, A. Onnela, A. P. Praplan, L. Rondo, F. D. Santos, S. Schallhart, R. Schnitzhofer, M. Sipilä, A. Tomé, G. Tsagkogeorgas, H. Vehkamäki, D. Wimmer, U. Baltensperger, K. S. Carslaw, J. Curtius, A. Hansel, T. Petäjä, M. Kulmala, N. M. Donahue, D. R. Worsnop, Molecular understanding of atmospheric particle formation from sulfuric acid and large oxidized organic molecules. *Proc. Natl. Acad. Sci. U.S.A.* **110**, 17223–17228 (2013). Medline doi:10.1073/pnas.1306973110

36. J. D. Crounse, L. B. Nielsen, S. Jørgensen, H. G. Kjaergaard, P. O. Wennberg, Autoxidation of organic compounds in the atmosphere. *J. Phys. Chem. Lett.* **4**, 3513–3520 (2013). doi:10.1021/jz4019207

37. M. Ehn, J. A. Thornton, E. Kleist, M. Sipilä, H. Junninen, I. Pullinen, M. Springer, F. Rubach, R. Tillmann, B. Lee, F. Lopez-Hilfiker, S. Andres, I.-H. Acir, M. Rissanen, T. Jokinen, S. Schobesberger, J. Kangasluoma, J. Kontkanen, T. Nieminen, T. Kurtén, L. B. Nielsen, S. Jørgensen, H. G. Kjaergaard, M. Canagaratna, M. D. Maso, T. Berndt, T. Petäjä, A. Wahner, V.-M. Kerminen, M. Kulmala, D. R. Worsnop, J. Wildt, T. F. Mentel, A large source of low-volatility secondary organic aerosol. *Nature* **506**, 476–479 (2014) Letter. Medline doi:10.1038/nature13032

38. M. E. Erupe, A. A. Viggiano, S.-H. Lee, The effect of trimethylamine on atmospheric nucleation involving H_2SO_4. *Atmos. Chem. Phys.* **11**, 4767–4775 (2011). doi:10.5194/acp-11-4767-2011

39. C. N. Jen, P. H. McMurry, D. R. Hanson, Stabilization of sulfuric acid dimers by ammonia, methylamine, dimethylamine, and trimethylamine. *J. Geophys. Res. Atmos.* **119**, 7502–7514 (2014). doi:10.1002/2014JD021592

40. T. Bergman, A. Laaksonen, H. Korhonen, J. Malila, E. Dunne, T. Mielonen, K. Lehtinen, T. Kühn, A. Arola, H. Kokkola, Geographical and diurnal features of amine-enhanced boundary layer nucleation. *J. Geophys. Res. Atmos.* **120**, 9606–9624 (2015). doi:10.1002/2015JD023181

41. X. Ge, A. S. Wexler, S. L. Clegg, Atmospheric amines − Part II. Thermodynamic properties and gas/particle partitioning. *Atmos. Environ.* **45**, 561–577 (2011). doi:10.1016/j.atmosenv.2010.10.013

42. J. Zhao, J. N. Smith, F. L. Eisele, M. Chen, C. Kuang, P. H. McMurry, Observation of neutral sulfuric acid-amine containing clusters in laboratory and ambient measurements. *Atmos. Chem. Phys.* **11**, 10823–10836 (2011). doi:10.5194/acp-11-10823-2011

43. D. V. Spracklen, K. S. Carslaw, J. Merikanto, G. W. Mann, C. L. Reddington, S. Pickering, J. A. Ogren, E. Andrews, U. Baltensperger, E. Weingartner, M. Boy, M. Kulmala, L. Laakso, H. Lihavainen, N. Kivekäs, M. Komppula, N. Mihalopoulos, G. Kouvarakis, S. G. Jennings, C. O'Dowd, W. Birmili, A. Wiedensohler, R. Weller, J. Gras, P. Laj, K. Sellegri, B. Bonn, R. Krejci, A. Laaksonen, A. Hamed, A. Minikin, R. M. Harrison, R. Talbot, J. Sun, Explaining global surface aerosol number concentrations in terms of primary emissions and particle formation. *Atmos. Chem. Phys.* **10**, 4775–4793 (2010). doi:10.5194/acp-10-4775-2010

44. A. D. Clarke, V. N. Kapustin, A Pacific aerosol survey, part I: A decade of data on particle production, transport, evolution, and mixing in the troposphere. *J. Atmos. Sci.* **59**, 363–382 (2002). doi:10.1175/1520-0469(2002)059<0363:APASPI>2.0.CO;2

45. A. D. Clarke, J. Varner, F. Eisele, R. Mauldin, D. Tanner, M. Litchy, Particle production in the remote marine atmosphere: Cloud outflow and subsidence during ACE 1. *J. Geophys. Res. Atmos.* **103**, 16397–16409 (1998). doi:10.1029/97JD02987

46. A. D. Clarke, F. Eisele, V. N. Kapustin, K. Moore, D. Tanner, L. Mauldin, M. Litchy, B. Lienert, M. Carroll, G. Albercook, Nucleation in the equatorial free troposphere:

Favorable environments during PEM-Tropics. *J. Geophys. Res. Atmos.* **104**, 5735–5744 (1999). [doi:10.1029/98JD02303](doi:10.1029/98JD02303)

47. L. A. Lee, K. J. Pringle, C. L. Reddington, G. W. Mann, P. Stier, D. V. Spracklen, J. R. Pierce, K. S. Carslaw, The magnitude and causes of uncertainty in global model simulations of cloud condensation nuclei. *Atmos. Chem. Phys.* **13**, 8879–8914 (2013). [doi:10.5194/acp-13-8879-2013](doi:10.5194/acp-13-8879-2013)

48. K. S. Carslaw, L. A. Lee, C. L. Reddington, G. W. Mann, K. J. Pringle, The magnitude and sources of uncertainty in global aerosol. *Faraday Discuss.* **165**, 495–512 (2013). Medline [doi:10.1039/c3fd00043e](doi:10.1039/c3fd00043e)

49. J. Kazil, K. Zhang, P. Stier, J. Feichter, U. Lohmann, K. O'Brien, The present-day decadal solar cycle modulation of Earth's radiative forcing via charged H_2SO_4/H_2O aerosol nucleation. *Geophys. Res. Lett.* **39**, L02805 (2012). [doi:10.1029/2011GL050058](doi:10.1029/2011GL050058)

50. J. R. Pierce, P. J. Adams, Can cosmic rays affect cloud condensation nuclei by altering new particle formation rates? *Geophys. Res. Lett.* **36**, L09820 (2009). [doi:10.1029/2009GL037946](doi:10.1029/2009GL037946)

51. A. F. Bouwman, D. Lee, W. Asman, F. Dentener, K. Van Der Hoek, J. Olivier, A global high-resolution emission inventory for ammonia. *Global Biogeochem. Cycles* **11**, 561–587 (1997). [doi:10.1029/97GB02266](doi:10.1029/97GB02266)

52. K. S. Carslaw, L. A. Lee, C. L. Reddington, K. J. Pringle, A. Rap, P. M. Forster, G. W. Mann, D. V. Spracklen, M. T. Woodhouse, L. A. Regayre, J. R. Pierce, Large contribution of natural aerosols to uncertainty in indirect forcing. *Nature* **503**, 67–71 (2013). Medline doi:10.1038/nature12674

53. U. Cubasch, D. Wuebbles, D. Chen, M. Facchini, D. Frame, N. Mahowald, J.-G. Winther, "Introduction," in *Climate Change 2013: The Physical Science Basis. Contribution of Working Group I to the Fifth Assessment Report of the IPCC*, T. F. Stocker *et al.*, Eds. (Cambridge Univ. Press, 2013), pp. 119–158.

54. F. Yu, G. Luo, R. P. Turco, J. A. Ogren, R. M. Yantosca, Decreasing particle number concentrations in a warming atmosphere and implications. *Atmos. Chem. Phys.* **12**, 2399–2408 (2012). [doi:10.5194/acp-12-2399-2012](doi:10.5194/acp-12-2399-2012)

55. P. Paasonen, A. Asmi, T. Petäjä, M. K. Kajos, M. Äijälä, H. Junninen, T. Holst, J. P. D. Abbatt, A. Arneth, W. Birmili, H. D. van der Gon, A. Hamed, A. Hoffer, L. Laakso, A. Laaksonen, W. Richard Leaitch, C. Plass-Dülmer, S. C. Pryor, P. Räisänen, E. Swietlicki, A. Wiedensohler, D. R. Worsnop, V.-M. Kerminen, M. Kulmala, Warming-induced increase in aerosol number concentration likely to moderate climate change. *Nat. Geosci.* **6**, 438–442 (2013). doi:10.1038/ngeo1800

56. R. Atkinson, D. L. Baulch, R. A. Cox, J. N. Crowley, R. F. Hampson, R. G. Hynes, M. E. Jenkin, M. J. Rossi, J. Troe, Evaluated kinetic and photochemical data for atmospheric chemistry: Volume I - gas phase reactions of O_x, HO_x, NO_x and SO_x species. *Atmos. Chem. Phys.* **4**, 1461–1738 (2004). [doi:10.5194/acp-4-1461-2004](doi:10.5194/acp-4-1461-2004)

57. A. Kupc, A. Amorim, J. Curtius, A. Danielczok, J. Duplissy, S. Ehrhart, H. Walther, L. Ickes, J. Kirkby, A. Kürten, J. M. Lima, S. Mathot, P. Minginette, A. Onnela, L. Rondo, P. E. Wagner, A fibre-optic UV system for H_2SO_4 production in aerosol chambers

causing minimal thermal effects. *J. Aerosol Sci.* **42**, 532–543 (2011). doi:10.1016/j.jaerosci.2011.05.001

58. J. Voigtländer, J. Duplissy, L. Rondo, A. Kürten, F. Stratmann, Numerical simulations of mixing conditions and aerosol dynamics in the CERN CLOUD chamber. *Atmos. Chem. Phys.* **12**, 2205–2214 (2012). doi:10.5194/acp-12-2205-2012

59. F. L. Eisele, D. Tanner, Measurement of the gas phase concentration of H_2SO_4 and methane sulfonic acid and estimates of H_2SO_4 production and loss in the atmosphere. *J. Geophys. Res. Atmos.* **98**, 9001–9010 (1993). doi:10.1029/93JD00031

60. A. Kürten, L. Rondo, S. Ehrhart, J. Curtius, Calibration of a chemical ionization mass spectrometer for the measurement of gaseous sulfuric acid. *J. Phys. Chem. A* **116**, 6375–6386 (2012). Medline doi:10.1021/jp212123n

61. T. Jokinen, M. Sipilä, H. Junninen, M. Ehn, G. Lönn, J. Hakala, T. Petäjä, R. L. Mauldin III, M. Kulmala, D. R. Worsnop, Atmospheric sulphuric acid and neutral cluster measurements using CI-APi-TOF. *Atmos. Chem. Phys.* **12**, 4117–4125 (2012). doi:10.5194/acp-12-4117-2012

62. A. Kürten, S. Münch, L. Rondo, F. Bianchi, J. Duplissy, T. Jokinen, H. Junninen, N. Sarnela, S. Schobesberger, M. Simon, M. Sipilä, J. Almeida, A. Amorim, J. Dommen, N. M. Donahue, E. M. Dunne, R. C. Flagan, A. Franchin, J. Kirkby, A. Kupc, V. Makhmutov, T. Petäjä, A. P. Praplan, F. Riccobono, G. Steiner, A. Tomé, G. Tsagkogeorgas, P. E. Wagner, D. Wimmer, U. Baltensperger, M. Kulmala, D. R. Worsnop, J. Curtius, Thermodynamics of the formation of sulfuric acid dimers in the binary (H_2SO_4-H_2O) and ternary (H_2SO_4-H_2O-NH_3) system. *Atmos. Chem. Phys.* **15**, 10701–10721 (2015). doi:10.5194/acp-15-10701-2015

63. S. Saunders, M. Jenkin, R. Derwent, M. Pilling, World wide web site of a master chemical mechanism (MCM) for use in tropospheric chemistry models. *Atmos. Environ.* **31**, 1249 (1997). doi:10.1016/S1352-2310(97)85197-7

64. F. Bianchi, J. Dommen, S. Mathot, U. Baltensperger, On-line determination of ammonia at low pptv mixing ratios in the CLOUD chamber. *Atmos. Meas. Tech.* **5**, 1719–1725 (2012). doi:10.5194/amt-5-1719-2012

65. A. P. Praplan, F. Bianchi, J. Dommen, U. Baltensperger, Dimethylamine and ammonia measurements with ion chromatography during the CLOUD4 campaign. *Atmos. Meas. Tech.* **5**, 2161–2167 (2012). doi:10.5194/amt-5-2161-2012

66. F. Bianchi, A. P. Praplan, N. Sarnela, J. Dommen, A. Kürten, I. K. Ortega, S. Schobesberger, H. Junninen, M. Simon, J. Tröstl, T. Jokinen, M. Sipilä, A. Adamov, A. Amorim, J. Almeida, M. Breitenlechner, J. Duplissy, S. Ehrhart, R. C. Flagan, A. Franchin, J. Hakala, A. Hansel, M. Heinritzi, J. Kangasluoma, H. Keskinen, J. Kim, J. Kirkby, A. Laaksonen, M. J. Lawler, K. Lehtipalo, M. Leiminger, V. Makhmutov, S. Mathot, A. Onnela, T. Petäjä, F. Riccobono, M. P. Rissanen, L. Rondo, A. Tomé, A. Virtanen, Y. Viisanen, C. Williamson, D. Wimmer, P. M. Winkler, P. Ye, J. Curtius, M. Kulmala, D. R. Worsnop, N. M. Donahue, U. Baltensperger, Insight into acid-base nucleation experiments by comparison of the chemical composition of positive, negative, and neutral clusters. *Environ. Sci. Technol.* **48**, 13675–13684 (2014). Medline doi:10.1021/es502380b

67. D. Wimmer, K. Lehtipalo, T. Nieminen, J. Duplissy, S. Ehrhart, J. Almeida, L. Rondo, A. Franchin, F. Kreissl, F. Bianchi, H. E. Manninen, M. Kulmala, J. Curtius, T. Petäjä, Technical Note: Using DEG-CPCs at upper tropospheric temperatures. *Atmos. Chem. Phys.* **15**, 7547–7555 (2015). [doi:10.5194/acp-15-7547-2015](doi:10.5194/acp-15-7547-2015)

68. V.-M. Kerminen, M. Kulmala, Analytical formulae connecting the 'real' and the 'apparent' nucleation rate and the nuclei number concentration for atmospheric nucleation events. *J. Aerosol Sci.* **33**, 609–622 (2002). [doi:10.1016/S0021-8502(01)00194-X](doi:10.1016/S0021-8502(01)00194-X)

69. S. Mirme, A. Mirme, The mathematical principles and design of the NAIS - a spectrometer for the measurement of cluster ion and nanometer aerosol size distributions. *Atmos. Meas. Tech.* **6**, 1061–1071 (2013). [doi:10.5194/amt-6-1061-2013](doi:10.5194/amt-6-1061-2013)

70. A. Kürten, C. Williamson, J. Almeida, J. Kirkby, J. Curtius, On the derivation of particle nucleation rates from experimental formation rates. *Atmos. Chem. Phys.* **15**, 4063–4075 (2015). [doi:10.5194/acp-15-4063-2015](doi:10.5194/acp-15-4063-2015)

71. J. J. Moré, *Numerical Analysis* (Springer, 1978), pp. 105–116.

72. I. K. Ortega, O. Kupiainen, T. Kurtén, T. Olenius, O. Wilkman, M. J. McGrath, V. Loukonen, H. Vehkamäki, From quantum chemical formation free energies to evaporation rates. *Atmos. Chem. Phys.* **12**, 225–235 (2012). [doi:10.5194/acp-12-225-2012](doi:10.5194/acp-12-225-2012)

73. I. K. Ortega, T. Olenius, O. Kupiainen-Määttä, V. Loukonen, T. Kurtén, H. Vehkamäki, Electrical charging changes the composition of sulfuric acid–ammonia/dimethylamine clusters. *Atmos. Chem. Phys.* **14**, 7995–8007 (2014). [doi:10.5194/acp-14-7995-2014](doi:10.5194/acp-14-7995-2014)

74. G. Brasseur, A. Chatel, paper presented at the 9th Annual Meeting of the European Geophysical Soceity, Leeds, Great Britain, August 1982 (1983).

75. V.-M. Kerminen, A. S. Wexler, Particle formation due to SO_2 oxidation and high relative humidity in the remote marine boundary layer. *J. Geophys. Res. Atmos.* **99**, 25607–25614 (1994). [doi:10.1029/94JD01988](doi:10.1029/94JD01988)

76. M. J. McGrath, T. Olenius, I. K. Ortega, V. Loukonen, P. Paasonen, T. Kurte'n, M. Kulmala, H. Vehkamäki, Atmospheric cluster dynamics code: A flexible method for solution of the birth-death equations. *Atmos. Chem. Phys.* **12**, 2345–2355 (2012). [doi:10.5194/acp-12-2345-2012](doi:10.5194/acp-12-2345-2012)

77. T. Olenius, S. Schobesberger, O. Kupiainen-Määttä, A. Franchin, H. Junninen, I. K. Ortega, T. Kurtén, V. Loukonen, D. R. Worsnop, M. Kulmala, H. Vehkamäki, Comparing simulated and experimental molecular cluster distributions. *Faraday Discuss.* **165**, 75–89 (2013). Medline [doi:10.1039/c3fd00031a](doi:10.1039/c3fd00031a)

78. D. V. Spracklen, K. J. Pringle, K. S. Carslaw, M. P. Chipperfield, G. W. Mann, A global offline model of size-resolved aerosol microphysics: II. Identification of key uncertainties. *Atmos. Chem. Phys.* **5**, 3233–3250 (2005). [doi:10.5194/acp-5-3233-2005](doi:10.5194/acp-5-3233-2005)

79. M. P. Chipperfield, New version of the TOMCAT/SLIMCAT off-line chemical transport model: Intercomparison of stratospheric tracer experiments. *Q. J. R. Meteorol. Soc.* **132**, 1179–1203 (2006). [doi:10.1256/qj.05.51](doi:10.1256/qj.05.51)

80. P. T. Manktelow, K. S. Carslaw, G. W. Mann, D. V. Spracklen, The impact of dust on sulfate aerosol, CN and CCN during an East Asian dust storm. *Atmos. Chem. Phys.* **10**, 365–382 (2010). doi:10.5194/acp-10-365-2010

81. A. J. Kettle, M. O. Andreae, Flux of dimethylsulfide from the oceans: A comparison of updated data sets and flux models. *J. Geophys. Res.* **105**, 26793–26808 (2000). doi:10.1029/2000JD900252

82. P. D. Nightingale, G. Malin, C. S. Law, A. J. Watson, P. S. Liss, M. I. Liddicoat, J. Boutin, R. C. Upstill-Goddard, In situ evaluation of air-sea gas exchange parameterizations using novel conservative and volatile tracers. *Glob. Biogeochem. Cycles* **14**, 373–387 (2000). doi:10.1029/1999GB900091

83. J. Cofala, M. Amann, Z. Klimont, K. Kupiainen, L. Höglund-Isaksson, Scenarios of global anthropogenic emissions of air pollutants and methane until 2030. *Atmos. Environ.* **41**, 8486–8499 (2007). doi:10.1016/j.atmosenv.2007.07.010

84. A. Guenther, C. N. Hewitt, D. Erickson, R. Fall, C. Geron, T. Graedel, P. Harley, L. Klinger, M. Lerdau, W. A. McKay, T. Pierce, B. Scholes, R. Steinbrecher, R. Tallamraju, J. Taylor, P. Zimmerman, A global model of natural volatile organic compound emissions. *J. Geophys. Res.* **100**, 8873 (1995). doi:10.1029/94JD02950

85. F. Dentener, S. Kinne, T. Bond, O. Boucher, J. Cofala, S. Generoso, P. Ginoux, S. Gong, J. J. Hoelzemann, A. Ito, L. Marelli, J. E. Penner, J.-P. Putaud, C. Textor, M. Schulz, G. R. van der Werf, J. Wilson, Emissions of primary aerosol and precursor gases in the years 2000 and 1750 prescribed data-sets for AeroCom. *Atmos. Chem. Phys.* **6**, 4321–4344 (2006). doi:10.5194/acp-6-4321-2006

86. E. Mårtensson, E. Nilsson, G. de Leeuw, L. Cohen, H.-C. Hansson, Laboratory simulations and parameterization of the primary marine aerosol production. *J. Geophys. Res. Atmos.* **108**, 4297 (2003). doi:10.1029/2002JD002263

87. E. C. Monahan, D. E. Spiel, K. L. Davidson, in *Oceanic Whitecaps*, E. C. Monahan, G. Mac Niocaill, Eds. (Springer, 1986), pp. 167–174.

88. S. L. Gong, A parameterization of sea-salt aerosol source function for sub- and super-micron particles. *Glob. Biogeochem. Cycles* **17**, 1097 (2003). doi:10.1029/2003GB002079

89. J. Ovadnevaite, A. Manders, G. de Leeuw, D. Ceburnis, C. Monahan, A.-I. Partanen, H. Korhonen, C. D. O'Dowd, A sea spray aerosol flux parameterization encapsulating wave state. *Atmos. Chem. Phys.* **14**, 1837–1852 (2014). doi:10.5194/acp-14-1837-2014

90. R. Atkinson, D. L. Baulch, R. A. Cox, R. F. Hampson, J. A. Kerr (Chairman), J. Troe; IUPAC Subcommittee on Gas Kinetic Data Evaluation for Atmospheric Chemistry, Evaluated kinetic and photochemical data for atmospheric chemistry: Supplement III. *J. Phys. Chem. Ref. Data* **18**, 881 (1989). doi:10.1063/1.555832

91. R. Atkinson, D. L. Baulch, R. A. Cox, J. N. Crowley, R. F. Hampson, R. G. Hynes, M. E. Jenkin, M. J. Rossi, J. Troe, IUPAC Subcommittee, Evaluated kinetic and photochemical data for atmospheric chemistry: Volume II: Gas phase reactions of organic species. *Atmos. Chem. Phys.* **6**, 3625–4055 (2006). doi:10.5194/acp-6-3625-2006

92. P. Tunved, H. Korhonen, J. Ström, H.-C. Hansson, K. E. J. Lehtinen, M. Kulmala, A pseudo-Lagrangian model study of the size distribution properties over Scandinavia: Transport from Aspvreten to Värriö. *Atmos. Chem. Phys. Discuss.* **4**, 7757–7794 (2004). doi:10.5194/acpd-4-7757-2004

93. G. W. Mann, K. S. Carslaw, D. V. Spracklen, D. A. Ridley, P. T. Manktelow, M. P. Chipperfield, S. J. Pickering, C. E. Johnson, Description and evaluation of GLOMAP-mode: A modal global aerosol microphysics model for the UKCA composition-climate model. *Geosci. Model Dev.* **3**, 519–551 (2010). doi:10.5194/gmd-3-519-2010

94. F. Benduhn, G. W. Mann, K. J. Pringle, D. O. Topping, G. McFiggans, K. S. Carslaw, Size-resolved simulations of the aerosol inorganic composition with the new hybrid dissolution solver HyDiS-1.0 – Description, evaluation and first global modelling results. *Geosci. Model Dev. Discuss.* **2016**, 1–54 (2016). doi:10.5194/gmd-2015-264

95. D. Topping, D. Lowe, G. McFiggans, Partial Derivative Fitted Taylor expansion: An efficient method for calculating gas-liquid equilibria in atmospheric aerosol particles: 1. Inorganic compounds. *J. Geophys. Res. Atmos.* **114**, D04304 (2009). doi:10.1029/2008JD010099

96. S. V. Krupa, Effects of atmospheric ammonia (NH_3) on terrestrial vegetation: A review. *Environ. Pollut.* **124**, 179–221 (2003). Medline doi:10.1016/S0269-7491(02)00434-7

97. K. von Bobrutzki, C. F. Braban, D. Famulari, S. K. Jones, T. Blackall, T. E. L. Smith, M. Blom, H. Coe, M. Gallagher, M. Ghalaieny, M. R. McGillen, C. J. Percival, J. D. Whitehead, R. Ellis, J. Murphy, A. Mohacsi, A. Pogany, H. Junninen, S. Rantanen, M. A. Sutton, E. Nemitz, Field intercomparison of eleven atmospheric ammonia measurement techniques. *Atmos. Meas.Tech.* **3**, 91–112 (2010). doi:10.5194/amt-3-91-2010

98. F. Hilton, R. Armante, T. August, C. Barnet, A. Bouchard, C. Camy-Peyret, V. Capelle, L. Clarisse, C. Clerbaux, P.-F. Coheur, A. Collard, C. Crevoisier, G. Dufour, D. Edwards, F. Faijan, N. Fourrie´, A. Gambacorta, M. Goldberg, V. Guidard, D. Hurtmans, S. Illingworth, N. Jacquinet-Husson, T. Kerzenmacher, D. Klaes, L. Lavanant, G. Masiello, M. Matricardi, A. McNally, S. Newman, E. Pavelin, S. Payan, E. Pe'quignot, S. Peyridieu, T. Phulpin, J. Remedios, P. Schlu¨ssel, C. Serio, L. Strow, C. Stubenrauch, J. Taylor, D. Tobin, W. Wolf, D. Zhou, Hyperspectral Earth observation from IASI: Five years of accomplishments. *Bull. Am. Meteorol. Soc.* **93**, 347–370 (2012). doi:10.1175/BAMS-D-11-00027.1

99. L. Clarisse, C. Clerbaux, F. Dentener, D. Hurtmans, P.-F. Coheur, Global ammonia distribution derived from infrared satellite observations. *Nat. Geosci.* **2**, 479–483 (2009). doi:10.1038/ngeo551

100. M. Van Damme, L. Clarisse, C. L. Heald, D. Hurtmans, Y. Ngadi, C. Clerbaux, A. J. Dolman, J. W. Erisman, P. F. Coheur, Global distributions, time series and error characterization of atmospheric ammonia (NH_3) from IASI satellite observations. *Atmos. Chem. Phys.* **14**, 2905–2922 (2014).

101. I. G. Usoskin, G. A. Kovaltsov, I. A. Mironova, Cosmic ray induced ionization model CRAC:CRII: An extension to the upper atmosphere. *J. Geophys. Res.* **115**, D10302 (2010). doi:10.1029/2009JD013142

102. A. C. Fraser-Smith, Centered and eccentric geomagnetic dipoles and their poles, 16001985. *Rev. Geophys.* **25**, 1–16 (1987). [doi:10.1029/RG025i001p00001](doi:10.1029/RG025i001p00001)

103. K. Zhang, J. Feichter, J. Kazil, H. Wan, W. Zhuo, A. D. Griffiths, H. Sartorius, W. Zahorowski, L. Ramonet, M. Schmidt, C. Yver, R. E. M. Neubert, E. G. Brunke, Radon activity in the lower troposphere and its impact on ionization rate: A global estimate using different radon emissions. *Atmos. Chem. Phys.* **11**, 7817–7838 (2011). [doi:10.5194/acp-11-7817-2011](doi:10.5194/acp-11-7817-2011)

104. B. A. Tinsley, The global atmospheric electric circuit and its effects on cloud microphysics. *Rep. Prog. Phys.* **71**, 066801 (2008). [doi:10.1088/0034-4885/71/6/066801](doi:10.1088/0034-4885/71/6/066801)

105. R. G. Harrison, The global atmospheric electrical circuit and climate. *Surv. Geophys.* **25**, 441–484 (2004). [doi:10.1007/s10712-004-5439-8](doi:10.1007/s10712-004-5439-8)

106. M. Kulmala, A. Laaksonen, L. Pirjola, Parameterizations for sulfuric acid/water nucleation rates. *J. Geophys. Res.* **103**, 8301–8307 (1998). [doi:10.1029/97JD03718](doi:10.1029/97JD03718)

107. M. D. Petters, S. M. Kreidenweis, A single parameter representation of hygroscopic growth and cloud condensation nucleus activity. *Atmos. Chem. Phys.* **7**, 1961–1971 (2007). [doi:10.5194/acp-7-1961-2007](doi:10.5194/acp-7-1961-2007)

108. C. E. Scott, A. Rap, D. V. Spracklen, P. M. Forster, K. S. Carslaw, G. W. Mann, K. J. Pringle, L. Kiveka¨s, M. Kulmala, H. Lihavainen, P. Tunved, The direct and indirect radiative effects of biogenic secondary organic aerosol. *Atmos. Chem. Phys.* **14**, 447–470 (2014). [doi:10.5194/acp-14-447-2014](doi:10.5194/acp-14-447-2014)

109. A. Nenes, J. H. Seinfeld, Parameterization of cloud droplet formation in global climate models. *J. Geophys. Res. Atmos.* **108**, 4415 (2003). [doi:10.1029/2002JD002911](doi:10.1029/2002JD002911)

110. C. Fountoukis, A. Nenes, Continued development of a cloud droplet formation parameterization for global climate models. *J. Geophys. Res. Atmos.* **110**, D11212 (2005). [doi:10.1029/2004JD005591](doi:10.1029/2004JD005591)

111. R. Morales, A. Nenes, H. Jonsson, R. C. Flagan, J. H. Seinfeld, Evaluation of an entraining droplet activation parameterization using in situ cloud data. *J. Geophys. Res. Atmos.* **116**, D15205 (2011). [doi:10.1029/2010JD015324](doi:10.1029/2010JD015324)

112. J. M. Edwards, A. Slingo, Studies with a flexible new radiation code. I: Choosing a configuration for a large-scale model. *Q. J. R. Meteorol. Soc.* **122**, 689–719 (1996). [doi:10.1002/qj.49712253107](doi:10.1002/qj.49712253107)

113. A. Rap, C. E. Scott, D. V. Spracklen, N. Bellouin, P. M. Forster, K. S. Carslaw, A. Schmidt, G. Mann, Natural aerosol direct and indirect radiative effects. *Geophys. Res. Lett.* **40**, 3297–3301 (2013). [doi:10.1002/grl.50441](doi:10.1002/grl.50441)

114. W. B. Rossow, R. A. Schiffer, Advances in understanding clouds from ISCCP. *Bull. Am. Meteorol. Soc.* **80**, 2261–2287 (1999). doi:10.1175/1520-0477(1999)080<2261:AIUCFI>2.0.CO;2

115. A. Schmidt, K. S. Carslaw, G. W. Mann, A. Rap, K. J. Pringle, D. V. Spracklen, M. Wilson, P. M. Forster, Importance of tropospheric volcanic aerosol for indirect radiative forcing of climate. *Atmos. Chem. Phys.* **12**, 7321–7339 (2012). [doi:10.5194/acp-12-7321-2012](doi:10.5194/acp-12-7321-2012)

116. F. Yu, G. Luo, Modeling of gaseous methylamines in the global atmosphere: Impacts of oxidation and aerosol uptake. *Atmos. Chem. Phys.* **14**, 12455–12464 (2014). doi:10.5194/acp-14-12455-2014

117. X. Ge, A. S. Wexler, S. L. Clegg, Atmospheric amines-Part I. A review. *Atmos. Environ.* **45**, 524–546 (2011). doi:10.1016/j.atmosenv.2010.10.012

118. D. V. Spracklen, K. S. Carslaw, M. Kulmala, V. M. Kerminen, G. W. Mann, S. L. Sihto, The contribution of boundary layer nucleation events to total particle concentrations on regional and global scales. *Atmos. Chem. Phys.* **6**, 5631–5648 (2006). doi:10.5194/acp-6-5631-2006

119. D. V. Spracklen, K. J. Pringle, K. S. Carslaw, G. W. Mann, P. Manktelow, J. Heintzenberg, Evaluation of a global aerosol microphysics model against size-resolved particle statistics in the marine atmosphere. *Atmos. Chem. Phys.* **7**, 2073–2090 (2007). doi:10.5194/acp-7-2073-2007

120. D. V. Spracklen, K. S. Carslaw, M. Kulmala, V.-M. Kerminen, S.-L. Sihto, I. Riipinen, J. Merikanto, G. W. Mann, M. P. Chipperfield, A. Wiedensohler, W. Birmili, H. Lihavainen, Contribution of particle formation to global cloud condensation nuclei concentrations. *Geophys. Res. Lett.* **35**, L06808 (2008). doi:10.1029/2007GL033038

121. C. L. Reddington, K. S. Carslaw, D. V. Spracklen, M. G. Frontoso, L. Collins, J. Merikanto, A. Minikin, T. Hamburger, H. Coe, M. Kulmala, P. Aalto, H. Flentje, C. Plass-Dülmer, W. Birmili, A. Wiedensohler, B. Wehner, T. Tuch, A. Sonntag, C. D. O'Dowd, S. G. Jennings, R. Dupuy, U. Baltensperger, E. Weingartner, H.-C. Hansson, P. Tunved, P. Laj, K. Sellegri, J. Boulon, J.-P. Putaud, C. Gruening, E. Swietlicki, P. Roldin, J. S. Henzing, M. Moerman, N. Mihalopoulos, G. Kouvarakis, V. Ždímal, N. Zíková, A. Marinoni, P. Bonasoni, R. Duchi, Primary versus secondary contributions to particle number concentrations in the European boundary layer. *Atmos. Chem. Phys.* **11**, 12007–12036 (2011). doi:10.5194/acp-11-12007-2011

122. A. D. Clarke, S. Howell, P. Quinn, T. Bates, J. Ogren, E. Andrews, A. Jefferson, A. Massling, O. Mayol-Bracero, H. Maring, D. Savoie, G. Cass, INDOEX aerosol: A comparison and summary of chemical, microphysical, and optical properties observed from land, ship, and aircraft. *J. Geophys. Res. Atmos.* **107**, 8033 (2002). doi:10.1029/2001JD000572

123. H. Singh, W. Brune, J. Crawford, D. Jacob, P. Russell, Overview of the summer 2004 Intercontinental Chemical Transport Experiment–North America (INTEX-A). *J. Geophys. Res. Atmos.* **111**, D24S01 (2006). doi:10.1029/2006JD007905

124. I. Faloona, S. Conley, B. Blomquist, A. Clarke, V. Kapustin, S. Howell, D. H. Lenschow, A. R. Bandy, Sulfur dioxide in the tropical marine boundary layer: Dry deposition and heterogeneous oxidation observed during the Pacific Atmospheric Sulfur Experiment. *J. Atmos. Chem.* **63**, 13–32 (2009). doi:10.1007/s10874-010-9155-0

125. D. J. Jacob, J. H. Crawford, H. Maring, A. D. Clarke, J. E. Dibb, L. K. Emmons, R. A. Ferrare, C. A. Hostetler, P. B. Russell, H. B. Singh, A. M. Thompson, G. E. Shaw, E. McCauley, J. R. Pederson, J. A. Fisher, The Arctic Research of the Composition of the Troposphere from Aircraft and Satellites (ARCTAS) mission: Design, execution, and first results. *Atmos. Chem. Phys.* **10**, 5191–5212 (2010). doi:10.5194/acp-10-5191-2010

126. R. Wood, C. R. Mechoso, C. S. Bretherton, R. A. Weller, B. Huebert, F. Straneo, B. A. Albrecht, H. Coe, G. Allen, G. Vaughan, P. Daum, C. Fairall, D. Chand, L. Gallardo Klenner, R. Garreaud, C. Grados, D. S. Covert, T. S. Bates, R. Krejci, L. M. Russell, S. de Szoeke, A. Brewer, S. E. Yuter, S. R. Springston, A. Chaigneau, T. Toniazzo, P. Minnis, R. Palikonda, S. J. Abel, W. O. J. Brown, S. Williams, J. Fochesatto, J. Brioude, K. N. Bower, The VAMOS Ocean-Cloud-Atmosphere-Land Study Regional Experiment (VOCALS-REx): Goals, platforms, and field operations. *Atmos. Chem. Phys.* **11**, 627–654 (2011). doi:10.5194/acp-11-627-2011

127. G. W. Mann, K. S. Carslaw, C. L. Reddington, K. J. Pringle, M. Schulz, A. Asmi, D. V. Spracklen, D. A. Ridley, M. T. Woodhouse, L. A. Lee, K. Zhang, S. J. Ghan, R. C. Easter, X. Liu, P. Stier, Y. H. Lee, P. J. Adams, H. Tost, J. Lelieveld, S. E. Bauer, K. Tsigaridis, T. P. C. van Noije, A. Strunk, D. Vignati, N. Bellouin, M. Dalvi, C. E. Johnson, T. Bergman, H. Kokkola, K. von Salzen, F. Yu, G. Luo, A. Petzold, J. Heintzenberg, A. Clarke, J. A. Ogren, J. Gras, U. Baltensperger, U. Kaminski, S. G. Jennings, C. D. O'Dowd, R. M. Harrison, D. C. S. Beddows, M. Kulmala, Y. Viisanen, V. Ulevicius, N. Mihalopoulos, V. Zdimal, M. Fiebig, H.-C. Hansson, E. Swietlicki, J. S. Henzing, Intercomparison and evaluation of global aerosol microphysical properties among AeroCom models of a range of complexity. *Atmos. Chem. Phys.* **14**, 4679–4713 (2014). doi:10.5194/acp-14-4679-2014

128. H. E. Manninen, T. Nieminen, E. Asmi, S. Gagné, S. Häkkinen, K. Lehtipalo, P. Aalto, M. Vana, A. Mirme, S. Mirme, U. Hõrrak, C. Plass-Dülmer, G. Stange, G. Kiss, A. Hoffer, N. Töró, M. Moerman, B. Henzing, G. de Leeuw, M. Brinkenberg, G. N. Kouvarakis, A. Bougiatioti, N. Mihalopoulos, C. O'Dowd, D. Ceburnis, A. Arneth, B. Svenningsson, E. Swietlicki, L. Tarozzi, S. Decesari, M. C. Facchini, W. Birmili, A. Sonntag, A. Wiedensohler, J. Boulon, K. Sellegri, P. Laj, M. Gysel, N. Bukowiecki, E. Weingartner, G. Wehrle, A. Laaksonen, A. Hamed, J. Joutsensaari, T. Petäjä, V. M. Kerminen, M. Kulmala, EUCAARI ion spectrometer measurements at 12 European sites analysis of new particle formation events. *Atmos. Chem. Phys.* **10**, 7907–7927 (2010). doi:10.5194/acp-10-7907-2010

129. F. Yu, G. Luo, S. C. Pryor, P. R. Pillai, S. H. Lee, J. Ortega, J. J. Schwab, A. G. Hallar, W. R. Leaitch, V. P. Aneja, J. N. Smith, J. T. Walker, O. Hogrefe, K. L. Demerjian, Spring and summer contrast in new particle formation over nine forest areas in North America. *Atmos. Chem. Phys.* **15**, 13993–14003 (2015). doi:10.5194/acp-15-13993-2015

130. J.-P. Pietikäinen, S. Mikkonen, A. Hamed, A. I. Hienola, W. Birmili, M. Kulmala, A. Laaksonen, Analysis of nucleation events in the European boundary layer using the regional aerosol-climate model REMO-HAM with a solar radiation-driven OH-proxy. *Atmos. Chem. Phys.* **14**, 11711–11729 (2014). doi:10.5194/acp-14-11711-2014

131. P. Paasonen, T. Nieminen, E. Asmi, H. E. Manninen, T. Petäjä, C. Plass-Dülmer, H. Flentje, W. Birmili, A. Wiedensohler, U. Hõrrak, A. Metzger, A. Hamed, A. Laaksonen, M. C. Facchini, V.-M. Kerminen, M. Kulmala, On the roles of sulphuric acid and low-volatility organic vapours in the initial steps of atmospheric new particle formation. *Atmos. Chem. Phys.* **10**, 11223–11242 (2010). doi:10.5194/acp-10-11223-2010

132. G. R. Van Der Werf, J. T. Randerson, G. J. Collatz, L. Giglio, Carbon emissions from fires in tropical and subtropical ecosystems. *Glob. Change Biol.* **9**, 547–562 (2003). doi:10.1046/j.1365-2486.2003.00604.x

133. P. Stier, J. Feichter, S. Kinne, S. Kloster, E. Vignati, J. Wilson, L. Ganzeveld, I. Tegen, M. Werner, Y. Balkanski, M. Schulz, O. Boucher, A. Minikin, A. Petzold, The aerosol-climate model ECHAM5- HAM. *Atmos. Chem. Phys.* **5**, 1125–1156 (2005). doi:10.5194/acp-5-1125-2005

134. T. C. Bond, D. G. Streets, K. F. Yarber, S. M. Nelson, J.-H. Woo, Z. Klimont, A technology-based global inventory of black and organic carbon emissions from combustion. *J. Geophys. Res. Atmos.* **109**, D14203 (2004). doi:10.1029/2003JD003697

135. R. Andres, A. Kasgnoc, A time-averaged inventory of subaerial volcanic sulfur emissions. *J. Geophys. Res. Atmos.* **103**, 25251–25261 (1998). doi:10.1029/98JD02091